Geomechanics for Energy and the Environment 4 (2015) 4–28

Contents lists available at ScienceDirect

Geomechanics for Energy and the Environment

journal homepage: www.elsevier.com/locate/gete

Analysis of delamination and damage growth in joined bi-layer systems

Z. Mróz *, K.P. Mróz

Institute of Fundamental Technological Research, Pawińskiego 5b, 02-106 Warsaw, Poland

HIGHLIGHTS

- The paper presents analytical solution of the delamination process in a bi-layer plate using the cohesive zone model.
- The effect of elastic moduli and softening moduli on the delamination process has been clarified.
- It was shown that the limit load value is related to fracture energy and stiffness moduli of adhering plates.
- The scale effect is analytically expressed.

ARTICLE INFO

Article history:
Received 24 June 2015
Received in revised form 7 October 2015
Accepted 7 October 2015
Available online 17 October 2015

Keywords:
Delamination
Cohesive zone
Shear lag
Damage process

ABSTRACT

The analysis of mechanical response of joined bi- or multi-layer systems is a typical problem for both geomechanics and composite technology. The elastic or visco-elastic layers interact through joining interfaces transferring stress state between layers and assuring structure integrity. The typical damage modes are related to progressive delamination at bonding interfaces, affected by distributed layer cracking. The present work is aimed to provide an analytical study of the stress state in a bi-layer system and of the progressive delamination process. The cohesive zone model is applied to simulate the interface response with shear stresses related to displacement discontinuities and to the specific fracture energies in shear mode. The following specific issues are discussed: delamination mode growth with the related critical and post-critical response of evaluation length of the process zone, scale effect of the critical stress. The analysis results can be applied to clarify the effect of material parameters on the damage process and to discuss experimental testing of epoxy joined ceramic elements, with specification of the connection strength, related to both the critical interface stress and the specific fracture energy.

1. Introduction

Coating layers are usually deposited on boundary surfaces of structural elements in order to improve their mechanical response, such as wear, corrosion or fatigue resistance. Due to mismatch of the thermo-mechanical properties of film–substrate systems the residual stresses are generated both in the initial and loaded states. The damage and failure in layered structures or coatings on substrate constitutes the most important class of problems for this type of composite materials. In most cases the delamination at interface and layer cracking are the main modes of degradation of structure performance. An extensive research has been conducted in the last period in this area, with application of different approaches generally based on the fracture mechanics models or on Cohesive Zone Model (CZM) approach. In the case of surface cracking the small cracks can nucleate from a surface defect but for low load they do not channel through the film. Thus, as a result, small cracks remain stable

* Corresponding author. Tel.: +48 22 826 12 81.
E-mail addresses: zmroz@ippt.pan.pl (Z. Mróz), kmroz@ippt.pan.pl (K.P. Mróz).

http://dx.doi.org/10.1016/j.gete.2015.10.001
2352-3808/

and can be tolerable for many applications. However, for higher stresses within the coating one observes a channeling process with a network of cracks surrounding islands of the intact film.[1] Upon reaching coating/substrate interface several failure mechanisms can follow: cracks enter the substrate material and stabilize at a certain depth.[2–4] They can also deviate and propagate along the coating/substrate interface resulting in a subsequent debonding of the protective film.[5,6] The substrate spalling is another intriguing phenomenon: the crack enters the substrate and selects a path at a certain depth parallel to the interface. This type of failure is common for brittle substrates.[7,8] The cracks arrested on the coating/substrate interface have been observed, also when cracks tend to interface under perpendicularly applied axial strain.[9–12] Then new cracks may appear during loading with initially increased crack density to stabilize at a fixed value, unaffected by further loading. This mode of failure is known as a segmentation or multiple cracking of thin films. The fundamental mode of failure, when the load causes the separation of the layers by generated interface cracks, is delamination directly associated with the fracture toughness.

The fracture mechanics models are usually based on Linear Elastic Fracture Mechanics (LEFM) and energy criteria, namely on the potential energy release rate as the generalized driving force specifying progressive crack growth at its critical value. In Ref. [10,13,14] the energy release rate has been derived in a closed form by applying the variational approach in crack analysis of coated and multilayer systems. In the analysis of segmentation cracking, Hu and Evans[15] assumed the constant shear stress value at the interface, corresponding to ductile response. The similar elastic-perfectly plastic model for the interface was applied by Timm et al.[16] to predict the crack spacing within asphalt pavements. A considerable efforts have been devoted to develop fracture mechanics of interfacial cracking. Hutchinson and Suo[17] provided an extensive study of the singular stress regime and of cracking modes along the interface combined with layer cracking. As the compliance discontinuity occurs, it affects the driving force and induces the local shear stresses at the crack tip. Due to the elastic mismatch the interface or near interface crack experiences both tensile and shear modes (Modes I and II) even if the remote loading corresponds to Mode I. Generally, the crack growth near or at the interface has been shown to depend on the relative strength of coating and substrate or the strength of interfacial bond relative to the strength of adjacent layers. Numerous studies have also been devoted to the fatigue failure of coated layers and correlation between the ability of cracks to traverse an interface undeflected and the bond strength of the interface.[18–22] Suresh and Sugimara successfully predicted the crack growth toward the interface in ductile-bimaterial systems by accounting for the constraint of plastic slip mechanisms ahead of the crack tip and adapted this approach to the analysis for crack growth in a system with brittle coatings.[23–26]

The LEFM solutions for interface cracks exhibit singular oscillatory behavior of stress field in the crack tip zone, generating some difficulties in crack growth modeling. An useful alternative to LEFM is the shear lag (SL) or the cohesive zone model (CZM). The shear lag approach has been frequently applied in the analysis of stress transfer through the interfacial shear stress in composite or bonded materials. The interface tractions τ_n, σ_n are then assumed to be related to displacement jumps u_t, u_n. The elastic analysis of rivet connected elements using this methods was initiated by Volkersen[27] in 1938 and later by Cox[28] in a simple one dimensional model of analysis of stress transfer between a matrix and a fiber assuming the linear elastic relation between shear stress and tangential slip. The subsequent treatments by Hedgepeth[29] and Kelly and Tyson[30] were devoted to composite analysis assuming elastic or elastic–plastic interaction models. The cohesive zone models (CZM) first proposed by Dugdale[31] and Barrenblatt[32] were addressed to analyze the localized damage or plastic flow in the front of crack tip. Next they have been developed to become an effective numerical tool for the analysis of crack initiation and growth, also for study of interfacial fracture of composites. In the literature, numerous proposals for the non-linear interaction between interface tractions and displacement jumps have been presented for the cohesive elements, such as trapezoidal,[33] perfectly plastic,[34] polynomial and exponential rules.[35,36] However, the most common and useful is the bilinear model, accounting for elastic and softening deformation stages preceding final failure. The cohesive zone models implemented in FEM have been widely exploited for specification of critical loads of bonded joints.[37,38] The interface problems and delamination failure were numerically analyzed in Ref. [39–42]. The comparative analysis of several cohesive models in predicting the onset of cracking and failure loads was presented in Ref. [42].

The analytical solutions for the cohesive zone models have been presented in several papers. The analytical treatment is important for the analysis of effect of material and geometric parameters on failure loads and their modes. The analytical solution of beam debonding form rigid substrate under normal load was presented by Williams and Hadivinia.[43] The problem of fiber pull-out for the assumed cohesive model was analytically treated by Schreyer and Peffer.[44] The delamination process under compressive normal load was treated by Mroz and Bialas,[45] next by Bialas and Mroz[46,47] indicating differing tangential deformation response due to coupling of delamination and sliding friction effects. The numerical treatment of cracking of surface coating layer in flexural mode was experimentally and numerically treated by Bialas et al.[48] Crack patterns in thin layers under temperature loading were studied analytically by Bialas and Mroz[48,49] presenting stress analysis and applying the total energy minimization method for prediction of crack pattern. The analytical solutions for specific cases of delamination process in a bi-material structure were presented by Ivanova et al.[50] and Nikolova et al.[51]

The objective of the present work is to provide the analytical treatment of the delamination process in a bilinear structure for the assumed linear elastic and linear damage relation between interface shear stress, τ_I and displacement jump u_I. The analytical solutions provide the insight into the initiation and growth of the damage

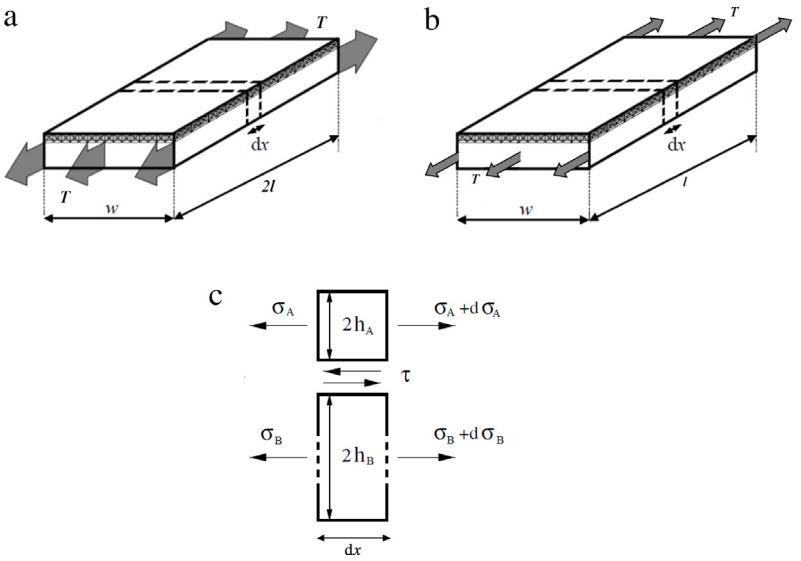

Fig. 1. (a) Bi-layer structure loaded by end forces on substrate plate (b) loaded lap-joint (c) stress acting on the infinitesimal bi-layer element.

process zone, crack initiation and growth length, leading to ultimate failure of the interface. The length evolution of the process zone along the interface is analyzed and compared with the predictions based on the fracture energy and critical stress concepts. Two cases are considered: first, the interface delamination for substrate plate loaded inducing delamination of the coating plate, next the lap joint failure process due to growth of delamination zones from two interface ends.

In Section 2 the problem formulation, governing equations and general solutions presenting displacement, and stress fields in both plates for different combination of elastic, softening and failure stress regimes are presented. The limiting cases for perfectly ductile or brittle response of bonding interface and plate are also considered. In Sections 3 and 4, the specific cases are considered when the increasing load is imposed. The analysis of progressive delamination is then presented. The analytical expression and diagrams illustrate the effect of geometric and material parameters on the damage mode in the bi-material system.

2. Problem formulation

Consider two plates A and B bonded along the interface I and loaded uniaxially at two opposite edges (Fig. 1). The thickness of plates is $2h_A$ and $2h_B$, where $2h_A$ corresponding to the coating layer is usually much smaller than the substrate plate thickness $2h_B$. The uniform in-plane loading induces tensile or compressive stress in plates A and B, bending and peel stresses are neglected. The elastic analysis of double lap joints by Goglio and Rosetto[52] with account for bending moments and peel stress indicates that this low value stress is compressive and does not affect the shear failure. The bonding interface is assumed to transfer shear stresses between two plates and its response is expressed in terms of displacement discontinuity of two plates. Denote the uniaxial stresses (uniform across the thickness) in plates by $\sigma_A = \sigma_A(x)$ and $\sigma_B = \sigma_B(x)$ and by $\tau_I = \tau_I(x)$ the interface shear stress. The following equilibrium equations can be written for the resulting forces $T_A(x) = 2h_A\sigma_A$ and $T_B(x) = 2h_B\sigma_B$

$$\frac{dT_A}{dx} = \tau_I, \qquad \frac{dT_B}{dx} = -\tau_I,$$
$$\text{or} \tag{1}$$
$$2h_A\frac{d\sigma_A}{dx} = \tau_I, \qquad 2h_B\frac{d\sigma_B}{dx} = -\tau_I,$$

where x denotes the position along the plate length. The displacement fields in plates are denoted by $u_A = u_A(x)$ and $u_B = u_B(x)$, the corresponding strains are

$$\varepsilon_A = \frac{du_A}{dx}, \qquad \varepsilon_B = \frac{du_B}{dx}. \tag{2}$$

The substrate plate is assumed to follow linear elastic response $\sigma_B = E_B\varepsilon_B$ and its Young modulus is E_B. The mechanical response of the coating plate A and of bonding interface is presented in (Fig. 2).

The coating layer A is assumed to deform initially, as a linear elastic material and after reaching the critical stress value σ_A^C the damage induced softening response follows until full failure. We can write

$$\sigma_A = \begin{cases} E_A\varepsilon_A & \text{for } \varepsilon_A \le \dfrac{\sigma_A^C}{E_A} = \varepsilon_A^C \\ \sigma_A^C - E_{As}(\varepsilon_A - \varepsilon_A^C) & \text{for } \varepsilon_A > \varepsilon_A^C \\ 0 & \text{for } \varepsilon_A \ge \varepsilon_A^f. \end{cases} \tag{3}$$

The similar interface response presented in (Fig. 2(a)) can be specified in terms of displacement discontinuity $u_I = u_A - u_B$. The shear strain in the bonding layer of

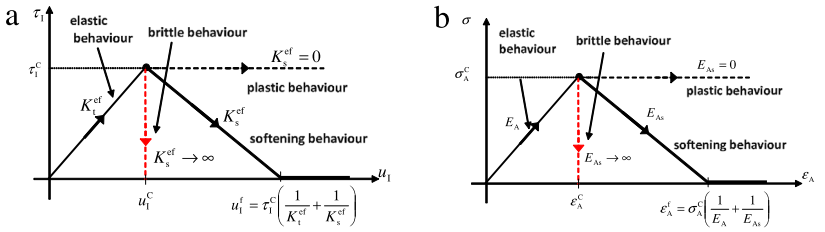

Fig. 2. The stress–strain models of (a) interface, (b) coating plate.

thickness h can be expressed as follows

$$\gamma = \frac{u_A - u_B}{h} = \frac{u_I}{h} \quad \text{and}$$

$$\tau_I = \begin{cases} K_t\gamma = \dfrac{K_t}{h}u_I = K_t^{ef}u_I \quad \text{for } u_I \le u_I^C = \dfrac{\tau_I^C}{K}, \\ \tau_I^C - \dfrac{K_s}{h}(u_I - u_I^C) = \tau_I^C - K_s^{ef}(u_I - u_I^C) \\ \quad \text{for } u_I > u_I^C. \\ 0 \quad \text{for } u_I \ge u_I^f \end{cases} \tag{4}$$

where, τ_I^C is the critical stress initiating failure through the softening response and u_I^C is the corresponding critical displacement discontinuity. Here the elastic shear and softening moduli are denoted by K_t and K_s. The thickness h of the bonding layer occurs only in the values of the effective shear moduli $K_t^{ef} = K_t/h$ and $K_s^{ef} = K_s/h$. Assuming the coating layer and interface responses as in Fig. 2, different cases can be analyzed. When $E_{As} = 0$, the fully ductile response of the layer A occurs. On the other hand, when $E_{As} = \infty$, the perfectly brittle response with immediate stress drops to zero value after reaching the critical stress, σ_A^C and the strain $\varepsilon_A^C = \varepsilon_A^f$. The similar ductile or brittle responses of the bonding interface can be described. The critical failure strain ε_A^f or the critical displacement discontinuity u_I^f at the state of total failure now are

$$\varepsilon_A^f = \sigma_A^C\left(\frac{1}{E_A} + \frac{1}{E_{As}}\right), \qquad u_I^f = \tau_I^C\left(\frac{1}{K_t^{ef}} + \frac{1}{K_s^{ef}}\right). \tag{5}$$

The total specific energy release due to coating layer or interface failure is

$$G_A = \frac{1}{2}\sigma_A^C\varepsilon_A^f = \frac{1}{2}(\sigma_A^C)^2\left(\frac{1}{E_A} + \frac{1}{E_{As}}\right),$$
$$G_I = \frac{1}{2}\tau_I^C u_I^f = \frac{1}{2}(\tau_I^C)^2\left(\frac{1}{K_t^{ef}} + \frac{1}{K_s^{ef}}\right). \tag{6}$$

Accounting for both layer and interface damage, different interactive regimes can be generated, as illustrated in Fig. 2. Assuming first two layers as elastic, only interface damage growth and delamination process can be analyzed. The present constitutive model assumptions follow the previous more general formulation of interface damage and failure model for mixed mode conditions in Ref.[45,46].

2.1. Elastic solution (E-E-E)

Consider now first the elastic responses of the coating (E), interface (E) and substrate (E) according to Fig. 3 and write the equilibrium equations (1) in the form

$$2h_AE_A\frac{d^2u_A}{dx^2} = K_t^{ef}u_I$$
$$2h_BE_B\frac{d^2u_B}{dx^2} = -K_t^{ef}u_I \tag{7}$$

where, the second derivatives result from (2) and (3). In view of (7), the following equation is easily derived for the displacement discontinuity $u_I = u_A - u_B$, thus

$$\frac{d^2u_I}{dx^2} = \lambda_e^2u_I, \tag{8}$$

where

$$\lambda_e^2 = K_t^{ef}\left(\frac{1}{2h_AE_A} + \frac{1}{2h_BE_B}\right) > 0. \tag{9}$$

The general integral of Eq. (8) has the form

$$u_I = C_1\sinh[\lambda_e x] + C_2\cosh[\lambda_e x], \tag{10}$$

where, C_1, C_2 are the integration constants. Having the form of $u_I(x)$, the stress and displacement fields of two layers are expressed by using the equilibrium equations (1) and the strain–displacement relations (2). We have

$$\begin{aligned} \tau_I &= K_t^{ef}(C_1\sinh[\lambda_e x] + C_2\cosh[\lambda_e x]), \\ T_A &= 2h_A\sigma_A = \frac{K_t^{ef}}{\lambda_e}(C_1\cosh[\lambda_e x] \\ &\quad + C_2\sinh[\lambda_e x]) + 2h_AC_3, \\ T_B &= 2h_B\sigma_B = -\frac{K_t^{ef}}{\lambda_e}(C_1\cosh[\lambda_e x] \\ &\quad + C_2\sinh[\lambda_e x]) - 2h_B\tilde{C}_3, \\ u_A &= \frac{K_t^{ef}}{2h_AE_A\lambda_e^2}(C_1\sinh[\lambda_e x] + C_2\cosh[\lambda_e x]) \\ &\quad + \frac{C_3}{E_A}x + C_4, \\ u_B &= -\frac{K_t^{ef}}{2h_BE_B\lambda_e^2}(C_1\sinh[\lambda_e x] + C_2\cosh[\lambda_e x]) \\ &\quad - \frac{\tilde{C}_3}{E_B}x + \tilde{C}_4, \end{aligned} \tag{11}$$

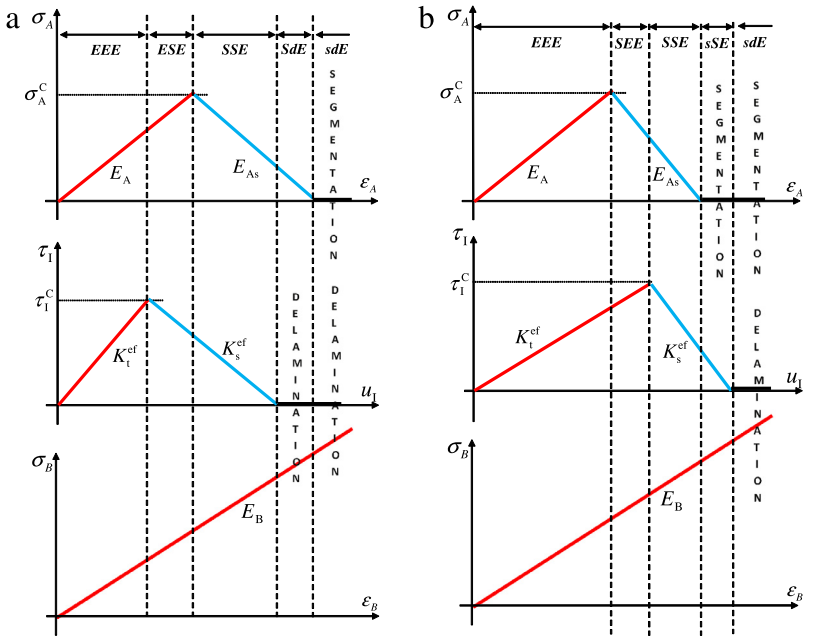

Fig. 3. Deformation models for coating-interface interaction.

where, C_3, $\tilde{C}_3$, C_4, $\tilde{C}_4$ are constants to be specified from the boundary and continuity conditions. However, requiring $u_\mathrm{I} = u_\mathrm{A} - u_\mathrm{B}$, the constants can be reduced, as follows: $\tilde{C}_4 = C_4$ and $\tilde{C}_3 = -E_\mathrm{B}/E_\mathrm{A}C_3$. Then,

$$\begin{aligned}
\tau_\mathrm{I} &= K_\mathrm{t}^\mathrm{ef}(C_1\sinh[\lambda_\mathrm{e}x] + C_2\cosh[\lambda_\mathrm{e}x]),\\
T_\mathrm{A} &= \frac{K_\mathrm{t}^\mathrm{ef}}{\lambda_\mathrm{e}}(C_1\cosh[\lambda_\mathrm{e}x] + C_2\sinh[\lambda_\mathrm{e}x]) + 2h_\mathrm{A}C_3,\\
T_\mathrm{B} &= -\frac{K_\mathrm{t}^\mathrm{ef}}{\lambda_\mathrm{e}}(C_1\cosh[\lambda_\mathrm{e}x] + C_2\sinh[\lambda_\mathrm{e}x])\\
&\quad + 2h_\mathrm{B}\frac{E_\mathrm{B}}{E_\mathrm{A}}C_3,\\
u_\mathrm{A} &= \frac{K_\mathrm{t}^\mathrm{ef}}{2h_\mathrm{A}E_\mathrm{A}\lambda_\mathrm{e}^2}(C_1\sinh[\lambda_\mathrm{e}x] + C_2\cosh[\lambda_\mathrm{e}x])\\
&\quad + \frac{C_3}{E_\mathrm{A}}x + C_4,\\
u_\mathrm{B} &= -\frac{K_\mathrm{t}^\mathrm{ef}}{2h_\mathrm{B}E_\mathrm{B}\lambda_\mathrm{e}^2}(C_1\sinh[\lambda_\mathrm{e}x] + C_2\cosh[\lambda_\mathrm{e}x])\\
&\quad + \frac{C_3}{E_\mathrm{A}}x + C_4.
\end{aligned} \tag{12}$$

2.2. Elastic plates-softening interface (E-S-E)

Assume first that plates are in the elastic state (E) and the interface in the softening state (S). Then we have

$$\begin{aligned}
\tau_\mathrm{I} &= \tau_\mathrm{I}^\mathrm{C} - K_\mathrm{s}^\mathrm{ef}(u_\mathrm{I} - u_\mathrm{I}^\mathrm{C}) = \left(1 + \frac{K_\mathrm{s}^\mathrm{ef}}{K_\mathrm{t}^\mathrm{ef}}\right)\tau_\mathrm{I}^\mathrm{C} - K_\mathrm{s}^\mathrm{ef}u_\mathrm{I}\\
&= A - K_\mathrm{s}^\mathrm{ef}u_\mathrm{I}
\end{aligned} \tag{13}$$

where the interface softening is beginning at $\tau_\mathrm{I}^\mathrm{C}$ value, as presented in Fig. 2(b). Then the equilibrium equations take the form

$$\begin{aligned}
2h_\mathrm{A}E_\mathrm{A}\frac{\mathrm{d}^2u_\mathrm{A}}{\mathrm{d}x^2} &= A - K_\mathrm{s}^\mathrm{ef}u_\mathrm{I},\\
2h_\mathrm{B}E_\mathrm{B}\frac{\mathrm{d}^2u_\mathrm{B}}{\mathrm{d}x^2} &= -A + K_\mathrm{s}^\mathrm{ef}u_\mathrm{I},
\end{aligned} \tag{14}$$

and the field $u_\mathrm{I}(x)$ is specified from the equation

$$\frac{\mathrm{d}^2u_\mathrm{I}}{\mathrm{d}x^2} + \lambda_\mathrm{s}^2u_\mathrm{I} = F, \tag{15}$$

where

$$\begin{aligned}
A &= \left(1 + \frac{K_\mathrm{s}^\mathrm{ef}}{K_\mathrm{t}^\mathrm{ef}}\right)\tau_\mathrm{I}^\mathrm{C},\\
\lambda_\mathrm{s}^2 &= K_\mathrm{s}^\mathrm{ef}\left(\frac{1}{2h_\mathrm{A}E_\mathrm{A}} + \frac{1}{2h_\mathrm{B}E_\mathrm{B}}\right) > 0\\
F &= \left(\frac{1}{2h_\mathrm{A}E_\mathrm{A}} + \frac{1}{2h_\mathrm{B}E_\mathrm{B}}\right)\left(1 + \frac{K_\mathrm{s}^\mathrm{ef}}{K_\mathrm{t}^\mathrm{ef}}\right)\tau_\mathrm{I}^\mathrm{C}\\
&= \frac{\lambda_\mathrm{s}^2}{K_\mathrm{s}^\mathrm{ef}}\left(1 + \frac{K_\mathrm{s}^\mathrm{ef}}{K_\mathrm{t}^\mathrm{ef}}\right)\tau_\mathrm{I}^\mathrm{C}.
\end{aligned} \tag{16}$$

The integral equation (15) is of the form

$$u_\mathrm{I} = D_1\sin[\lambda_\mathrm{s}x] + D_2\cos[\lambda_\mathrm{s}x] + \frac{F}{\lambda_\mathrm{s}^2}. \tag{17}$$

The stress and displacement fields are now expressed as follows

$$
\begin{aligned}
\tau_{\mathrm{I}} &= -K_{\mathrm{s}}^{\mathrm{ef}}(D_1\sin[\lambda_{\mathrm{s}}x]+D_2\cos[\lambda_{\mathrm{s}}x]),\\
T_{\mathrm{A}} &= \frac{K_{\mathrm{s}}^{\mathrm{ef}}}{\lambda_{\mathrm{s}}}(D_1\cos[\lambda_{\mathrm{s}}x]-D_2\sin[\lambda_{\mathrm{s}}x])+2D_3h_{\mathrm{A}},\\
T_{\mathrm{B}} &= \frac{K_{\mathrm{s}}^{\mathrm{ef}}}{\lambda_{\mathrm{s}}}(-D_1\cos[\lambda_{\mathrm{s}}x]+D_2\sin[\lambda_{\mathrm{s}}x])-2\tilde{D}_3h_{\mathrm{B}},\\
u_{\mathrm{A}} &= \frac{K_{\mathrm{s}}^{\mathrm{ef}}}{2h_{\mathrm{A}}E_{\mathrm{A}}\lambda_{\mathrm{s}}^2}(D_1\sin[\lambda_{\mathrm{s}}x]+D_2\cos[\lambda_{\mathrm{s}}x])\\
&\quad+\frac{D_3}{E_{\mathrm{A}}}x+D_4,\\
u_{\mathrm{B}} &= \frac{K_{\mathrm{s}}^{\mathrm{ef}}}{2h_{\mathrm{B}}E_{\mathrm{B}}\lambda_{\mathrm{s}}^2}(-D_1\sin[\lambda_{\mathrm{s}}x]-D_2\cos[\lambda_{\mathrm{s}}x])\\
&\quad-\frac{\tilde{D}_3}{E_{\mathrm{B}}}x+\tilde{D}_4,
\end{aligned}
\tag{18}
$$

where, $D_1, D_2, D_3, D_4, \tilde{D}_3, \tilde{D}_4$ are constants. However, requiring $u_{\mathrm{I}} = u_{\mathrm{A}} - u_{\mathrm{B}}$, the constants can be reduced, as follows: $\tilde{D}_4 = D_4 - F/\lambda_{\mathrm{s}}^2$ and $\tilde{D}_3 = -E_{\mathrm{B}}/E_{\mathrm{A}}D_3$. Then,

$$
\begin{aligned}
\tau_{\mathrm{I}} &= -K_{\mathrm{s}}^{\mathrm{ef}}(D_1\sin[\lambda_{\mathrm{s}}x]+D_2\cos[\lambda_{\mathrm{s}}x]),\\
T_{\mathrm{A}} &= \frac{K_{\mathrm{s}}^{\mathrm{ef}}}{\lambda_{\mathrm{s}}}(D_1\cos[\lambda_{\mathrm{s}}x]-D_2\sin[\lambda_{\mathrm{s}}x])+2h_{\mathrm{A}}D_3,\\
T_{\mathrm{B}} &= \frac{K_{\mathrm{s}}^{\mathrm{ef}}}{\lambda_{\mathrm{s}}}(-D_1\cos[\lambda_{\mathrm{s}}x]+D_2\sin[\lambda_{\mathrm{s}}x])\\
&\quad+2h_{\mathrm{B}}E_{\mathrm{B}}/E_{\mathrm{A}}D_3,\\
u_{\mathrm{A}} &= \frac{K_{\mathrm{s}}^{\mathrm{ef}}}{2h_{\mathrm{A}}E_{\mathrm{A}}\lambda_{\mathrm{s}}^2}(D_1\sin[\lambda_{\mathrm{s}}x]-D_2\cos[\lambda_{\mathrm{s}}x])\\
&\quad+\frac{D_3}{E_{\mathrm{A}}}x+D_4,\\
u_{\mathrm{B}} &= \frac{K_{\mathrm{s}}^{\mathrm{ef}}}{2h_{\mathrm{B}}E_{\mathrm{B}}\lambda_{\mathrm{s}}^2}(-D_1\sin[\lambda_{\mathrm{s}}x]-D_2\cos[\lambda_{\mathrm{s}}x])\\
&\quad+\frac{D_3}{E_{\mathrm{A}}}x+D_4-F/\lambda_{\mathrm{s}}^2.
\end{aligned}
\tag{19}
$$

The proper continuity conditions should be stated to match different stress and displacement regimes. The continuity of forces $[T_{\mathrm{A}}] = [T_{\mathrm{B}}] = 0$ at the transition point require that $[u_{\mathrm{A}}] = [u_{\mathrm{B}}] = 0$, $[u'_{\mathrm{A}}] = [u'_{\mathrm{B}}] = 0$. These conditions can also be expressed as follows

$$
[u_{\mathrm{I}}] = [u'_{\mathrm{I}}] = 0, \qquad [T_{\mathrm{A}}] = 0, \qquad [u_{\mathrm{A}}] = 0. \tag{20}
$$

In fact, for the bi-layer structure loaded axially at its end, the condition $T_{\mathrm{A}} + T_{\mathrm{B}} = T$ occurs, where T is the resultant boundary load. Thus, it suffices to specify u_{I}, next force and displacement in one layer, say A. Then force and displacement in the second layer B are determined in terms of u_{I}, force T_{A} and displacement u_{A}.

The case

$$
u_{\mathrm{I}} = \tau_{\mathrm{I}} = 0 \tag{21}
$$

corresponds to *uniform force distribution* within both layers. As then $\varepsilon_{\mathrm{A}} = \varepsilon_{\mathrm{B}}$, $T_{\mathrm{A}} + T_{\mathrm{B}} = T$, we have

$$
T_{\mathrm{A}} = \frac{\rho}{1+\rho}T, \qquad T_{\mathrm{B}} = \frac{1}{1+\rho}T, \qquad \rho = \frac{2h_{\mathrm{A}}E_{\mathrm{A}}}{2h_{\mathrm{B}}E_{\mathrm{B}}} \tag{22}
$$

and the forces T_{A} and T_{B} are specified in terms of the boundary load T and the layer stiffness ratio ρ. The state (22) will be called the uniform stress state. It is important state for a multilayer system, as the local stress state affected by boundary conditions or imperfections (layer cracks, debonded spots) tends to the uniform state (22) for increasing distance from the stress perturbation source.

3. Substrate plate loading

3.1. Elastic analysis

Consider now the case of the substrate plate B loaded at both ends by the force $T_{\mathrm{B}}(l) = T_{\mathrm{B}}(-l) = T$ and the coating plate A with stress-free ends, $T_{\mathrm{A}}(l) = T_{\mathrm{A}}(-l) = 0$, Fig. 4. The plates are bonded along the interface layer I, whose thickness h is included in the definition of effective stiffness and softening layer moduli. As the boundary condition does not satisfy the uniform state condition (22), the interface shear stress $\tau_{\mathrm{I}}(x)$ is generated. Introducing the coordinate system x, y with its origin at the plate center and applying (12) with the boundary and symmetry conditions as

$$
T_{\mathrm{A}}(l) = 0, \qquad T_{\mathrm{B}}(l) = T, \qquad u_{\mathrm{I}}(0) = 0 \tag{23}
$$

we obtain

$$
\begin{aligned}
&C_1 = -\frac{\rho}{1+\rho}T\frac{\lambda_{\mathrm{e}}}{K_{\mathrm{t}}^{\mathrm{ef}}}\frac{1}{\cosh[\lambda_{\mathrm{e}}l]}, \qquad C_2 = 0,\\
&C_3 = \frac{\rho}{1+\rho}\frac{T}{2h_{\mathrm{A}}}
\end{aligned}
\tag{24}
$$

and the mechanical field is expressed as follows

$$
\begin{aligned}
u_{\mathrm{I}}^{\mathrm{e}}(x) &= -\frac{\rho}{1+\rho}T\frac{\lambda_{\mathrm{e}}}{K_{\mathrm{t}}^{\mathrm{ef}}}\frac{\sinh[\lambda_{\mathrm{e}}x]}{\cosh[\lambda_{\mathrm{e}}l]},\\
\tau_{\mathrm{I}}^{\mathrm{e}}(x) &= -\frac{\rho}{1+\rho}T\lambda_{\mathrm{e}}\frac{\sinh[\lambda_{\mathrm{e}}x]}{\cosh[\lambda_{\mathrm{e}}l]},\\
T_{\mathrm{A}}^{\mathrm{e}}(x) &= \frac{\rho}{1+\rho}T\left(1-\frac{\cosh[\lambda_{\mathrm{e}}x]}{\cosh[\lambda_{\mathrm{e}}l]}\right),\\
T_{\mathrm{B}}^{\mathrm{e}}(x) &= \frac{1}{1+\rho}T\left(1+\rho\frac{\cosh[\lambda_{\mathrm{e}}x]}{\cosh[\lambda_{\mathrm{e}}l]}\right).
\end{aligned}
\tag{25}
$$

Let us note that for increasing plate length, $\cosh[\lambda_{\mathrm{e}}l] \to \infty$ and the ratio $T_{\mathrm{A}}^{\mathrm{e}}(0)/T_{\mathrm{B}}^{\mathrm{e}}(0)$ tends to ρ, corresponding to the uniform stress regime. The displacement field for the boundary conditions $u_{\mathrm{A}}^{\mathrm{e}}(0) = u_{\mathrm{B}}^{\mathrm{e}}(0) = 0$ is obtained in the form

$$
\begin{aligned}
u_{\mathrm{B}}^{\mathrm{e}}(x) &= \int_0^x \frac{T_{\mathrm{B}}^{\mathrm{e}}(x)}{2h_{\mathrm{B}}E_{\mathrm{B}}}\mathrm{d}x\\
&= \frac{T}{2E_{\mathrm{B}}h_{\mathrm{B}}}\frac{1}{1+\rho}\left(x+\frac{\rho}{\lambda_{\mathrm{e}}}\frac{\sinh[\lambda_{\mathrm{e}}x]}{\cosh[\lambda_{\mathrm{e}}l]}\right)\\
u_{\mathrm{A}}^{\mathrm{e}}(x) &= u_{\mathrm{A}}^{\mathrm{e}}(x) + u_{\mathrm{I}}^{\mathrm{e}}(x)\\
&= \frac{T}{2E_{\mathrm{A}}h_{\mathrm{A}}}\frac{\rho}{1+\rho}\left(x-\frac{1}{\lambda_{\mathrm{e}}}\frac{\sinh[\lambda_{\mathrm{e}}x]}{\cosh[\lambda_{\mathrm{e}}l]}\right).
\end{aligned}
\tag{26}
$$

The interface damage initiation starts when $\tau_{\mathrm{I}}^{\mathrm{e}}(l) = \tau_{\mathrm{I}}^{\mathrm{C}}$. The acting critical load then equals

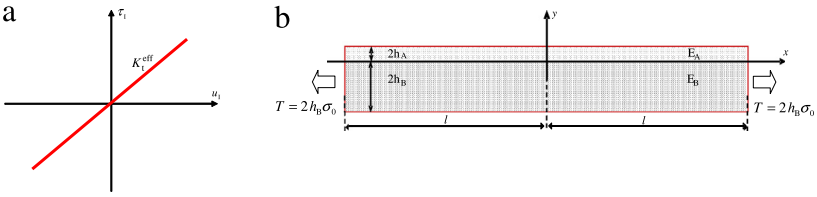

Fig. 4. Elastic interface model (a), mechanical loading (b).

$$T^C = T_B(l) = \frac{1+\rho}{\rho}\frac{\tau_l^C}{\lambda_e}\coth[\lambda_e l]. \tag{27}$$

Fig. 5(a), (b) present the distributions of forces T_A, T_B and of the interface stress, τ_l, for constant value of τ_l^C and varying values of stiffness parameter λ_e. It is seen that for increasing values λ_e, that is the ratio of shear stiffness of bonding layer to tension stiffness of plates, the shear stress near the boundary increases and the value of the critical load expressed by (27) decreases. Fig. 5(c) presents the dependence of critical load T^C initiating the delamination process on the plate length. It is seen that for increasing length the critical load tends to its asymptotic value $\frac{1+\rho}{\rho}\frac{\tau_l^C}{\lambda_e}$ which vanishes for $\lambda_e \to \infty$. The diagram $T^C - \lambda_e l$ specifies two domains of delamination and of no delamination.

3.2. Growth of process zone

For the elastic shear stress $\tau_l > |\tau_l^C|$, the symmetric damage process zones start to grow from two ends of plates. In view of symmetry, consider only the solution for $0 \le x \le l$. Assume the elastic zone to exist in the central domain $0 \le x \le l_e$ and the damage process zone in the boundary domain $l_e \le x \le l$, Fig. 6(b), with its initial growing length $d_p = l - l_e$. Fig. 6(b) presents schematically the shear stress field in two zones.

Using formulae (12) and (19) the mechanical states in two zones are expressed as follows.

Elastic zone: $0 \leqslant x \leqslant l_e$. The conditions $\tau_l^e(0) = 0$ requires that the integration constant $C_2 = 0$ and then we have

$$\begin{aligned}
\tau_l^e(x) &= K_t^{ef} C_1 \sinh[\lambda_e x],\\
T_A^e(x) &= \frac{K_t^{ef}}{\lambda_e} C_1 \cosh[\lambda_e x] + \frac{\rho}{1+\rho}T(l),\\
T_B^e(x) &= -\frac{K_t^{ef}}{\lambda_e} C_1 \cosh[\lambda_e x] + \frac{1}{1+\rho}T(l).
\end{aligned} \tag{28}$$

Damage process zone: $l_e \leqslant x \leqslant l$

$$\begin{aligned}
u_l^p(x) &= D_1 \sin[\lambda_s x] + D_2 \cos[\lambda_s x] + u_l^f,\\
\tau_l^p(x) &= -K_s^{ef}(D_1 \sin[\lambda_s x] + D_2 \cos[\lambda_s x]),\\
T_A^p(x) &= \frac{K_s^{ef}}{\lambda_s}(D_1 \cos[\lambda_s x] - D_2 \sin[\lambda_s x])\\
&\quad + \frac{\rho}{1+\rho}T(l),\\
T_B^p(x) &= \frac{K_s^{ef}}{\lambda_s}(-D_1 \cos[\lambda_s x] + D_2 \sin[\lambda_s x])\\
&\quad + \frac{1}{1+\rho}T(l),
\end{aligned} \tag{29}$$

where u_l^f is defined by (5). Satisfying the conditions $T_A^p(l) = 0$, $\tau_l^e(l_e) = \tau_l^p(l_e) = -\tau_l^C$, the integration constants are specified, namely

$$\begin{aligned}
C_1 &= -\frac{\tau_l^C}{K_t^{ef}}\frac{1}{\sinh[\lambda_e l_e]},\\
D_1 &= \frac{1}{\cos[\lambda_s(l-l_e)]}\left[-\frac{\rho}{1+\rho}T(l)\frac{\lambda_s}{K_s^{ef}}\cos[\lambda_s l_e]\right.\\
&\quad \left. + \frac{\tau_l^C}{K_s^{ef}}\sin[\lambda_s l]\right],\\
D_2 &= \frac{1}{\cos[\lambda_s(l-l_e)]}\left[\frac{\rho}{1+\rho}T(l)\frac{\lambda_s}{K_s^{ef}}\sin[\lambda_s l_e]\right.\\
&\quad \left. + \frac{\tau_l^C}{K_s^{ef}}\cos[\lambda_s l]\right].
\end{aligned} \tag{30}$$

Satisfying the continuity condition $[T_A(l_e)] = 0$, the relation is obtained specifying the length of the initial process zone $d_p = l - l_e$

$$\frac{T}{\tau_l^C}\frac{\rho}{1+\rho} = \frac{\sin[\lambda_s d_p]}{\lambda_s} + \frac{\coth[\lambda_e l_e]\cos[\lambda_s d_p]}{\lambda_e}. \tag{31}$$

Finally, the mechanical fields are in the elastic zone $0 \leqslant x \leqslant l_e$:

$$\begin{aligned}
\tau_l^e(x) &= -\tau_l^C\frac{\sinh[\lambda_e x]}{\sinh[\lambda_e l_e]},\\
T_A^e(x) &= -\frac{\tau_l^C}{\lambda_e}\frac{\cosh[\lambda_e x]}{\sinh[\lambda_e l_e]} + \frac{\rho}{1+\rho}T(l),\\
T_B^e(x) &= \frac{\tau_l^C}{\lambda_e}\frac{\cosh[\lambda_e x]}{\sinh[\lambda_e l_e]} + \frac{1}{1+\rho}T(l)
\end{aligned} \tag{32}$$

in the damage zone $l_e \leqslant x \leqslant l$:

$$\begin{aligned}
\tau_l^p(x) &= \frac{\sin[\lambda_s x]}{\cos[\lambda_s(l-l_e)]}\left[\frac{\rho}{1+\rho}T(l)\lambda_s\cos[\lambda_s l_e]\right.\\
&\quad \left. - \tau_l^C\sin[\lambda_s l]\right] - \frac{\cos[\lambda_s x]}{\cos[\lambda_s(l-l_e)]}\\
&\quad \times\left[\frac{\rho}{1+\rho}T(l)\lambda_s\sin[\lambda_s l_e] + \tau_l^C\cos[\lambda_s l]\right],\\
T_A^p(x) &= \frac{\cos[\lambda_s x]}{\cos[\lambda_s(l-l_e)]}\left[-\frac{\rho}{1+\rho}T(l)\cos[\lambda_s l_e]\right.\\
&\quad \left. + \frac{\tau_l^C}{\lambda_s}\sin[\lambda_s l]\right] - \frac{\sin[\lambda_s x]}{\cos[\lambda_s(l-l_e)]}
\end{aligned}$$

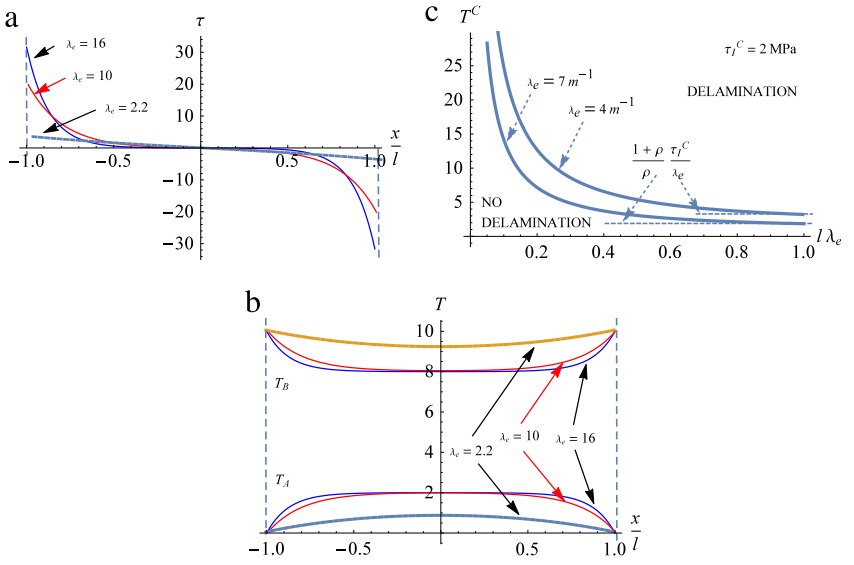

Fig. 5. Elastic distributions of the shear stress $\tau_{\mathrm{l}}(x)$, (a); of forces $T_{\mathrm{A}}(x)$, $T_{\mathrm{B}}(x)$, (b); critical force initiating the delamination process versus non-dimensional $\lambda_{\mathrm{e}} l$ values, (c).

$$u_{\mathrm{B}}^{\mathrm{e}}(x) = \frac{\lambda_{\mathrm{e}}^2 Tx + (1+\rho)\tau_{\mathrm{l}}^{\mathrm{C}} \sinh[\lambda_{\mathrm{e}} x]}{2E_{\mathrm{B}} h_{\mathrm{B}} \lambda_{\mathrm{e}}^2 (1+\rho) \sinh[\lambda_{\mathrm{e}} l_{\mathrm{e}}]}$$

$$u_{\mathrm{B}}^{\mathrm{p}}(x) = \frac{(\lambda_{\mathrm{e}}^2 + \lambda_{\mathrm{s}}^2)(1+\rho)\tau_{\mathrm{l}}^{\mathrm{C}} + \lambda_{\mathrm{e}}^2 \lambda_{\mathrm{s}}^2 Tx - \lambda_{\mathrm{e}}^2 \dfrac{\left[(1+\rho)\tau_{\mathrm{l}}^{\mathrm{C}} \cos[\lambda_{\mathrm{s}}(l-x)] + \lambda_{\mathrm{s}} \rho T \sin[\lambda_{\mathrm{s}}(l_{\mathrm{e}}-x)]\right]}{\cos[\lambda_{\mathrm{s}}(-l_{\mathrm{e}}+l)]}}{2E_{\mathrm{B}} h_{\mathrm{B}} \lambda_{\mathrm{e}}^2 \lambda_{\mathrm{s}}^2 (1+\rho)}. \tag{34}$$

Box I.

$$\times \left[\frac{\rho}{1+\rho} T(l) \sin[\lambda_{\mathrm{s}} l_{\mathrm{e}}] + \frac{\tau_{\mathrm{l}}^{\mathrm{C}}}{\lambda_{\mathrm{s}}} \cos[\lambda_{\mathrm{s}} l] \right]$$

$$+ \frac{\rho}{1+\rho} T(l), \tag{33}$$

$$T_{\mathrm{B}}^{\mathrm{p}}(x) = \frac{\cos[\lambda_{\mathrm{s}} x]}{\cos[\lambda_{\mathrm{s}}(l-l_{\mathrm{e}})]} \left[\frac{\rho}{1+\rho} T(l) \cos[\lambda_{\mathrm{s}} l_{\mathrm{e}}] - \frac{\tau_{\mathrm{l}}^{\mathrm{C}}}{\lambda_{\mathrm{s}}} \sin[\lambda_{\mathrm{s}} l] \right] + \frac{\sin[\lambda_{\mathrm{s}} x]}{\cos[\lambda_{\mathrm{s}}(l-l_{\mathrm{e}})]}$$

$$\times \left[\frac{\rho}{1+\rho} T(l) \sin[\lambda_{\mathrm{s}} l_{\mathrm{e}}] + \frac{\tau_{\mathrm{l}}^{\mathrm{C}}}{\lambda_{\mathrm{s}}} \cos[\lambda_{\mathrm{s}} l] \right]$$

$$+ \frac{1}{1+\rho} T(l).$$

The displacement of the plate B satisfying the boundary condition $u_{\mathrm{B}}^{\mathrm{e}}(0) = 0$ and the continuity condition $[u_{\mathrm{B}}(l_{\mathrm{e}})] = 0$ is expressed in two zones as Eq. (34) given in Box I.

3.2.1. Growth of delamination zone

The full delamination starts when $\tau_{\mathrm{l}}^{\mathrm{p}}(l) = 0$ and next the full delamination zone $d = d_{\mathrm{l}} - d_{\mathrm{p}} = l - l_{\mathrm{d}}$ grows from both ends, Fig. 6(b). From (32), setting $\tau_{\mathrm{l}}^{\mathrm{p}}(l) = 0$, we obtain the load at the onset of delamination

$$T = \frac{\rho+1}{\rho} \frac{\tau_{\mathrm{l}}^{\mathrm{C}}}{\lambda_{\mathrm{s}}} \frac{1}{\sin[\lambda_{\mathrm{s}} d_{\mathrm{p}}]}, \tag{35}$$

where, the value of d_{p} is specified from (31).

In the subsequent stage there are the delamination and damage process zones of lengths d and d_{p} evolving during the loading process, with the total damaged zone $d_{\mathrm{l}} = d_{\mathrm{p}} + d$. In the delaminated zone, the mechanical state is as follows

$$l_{\mathrm{d}} \leqslant x \leqslant l : T_{\mathrm{A}} = 0, \qquad T_{\mathrm{B}} = T, \qquad \tau_{\mathrm{l}} = 0. \tag{36}$$

In the process zone: $l_{\mathrm{e}} \leqslant x \leqslant l_{\mathrm{d}}$ the same relations as in Eq. (29) apply and the following boundary conditions are stated $T_{\mathrm{A}}^{\mathrm{p}}(l_{\mathrm{d}}) = 0$, $\tau_{\mathrm{l}}^{\mathrm{p}}(l_{\mathrm{d}}) = 0$ and the constants are

$$D_1 = -\frac{\rho}{1+\rho} T \frac{\lambda_{\mathrm{s}}}{K_{\mathrm{s}}^{\mathrm{ef}}} \cos[\lambda_{\mathrm{s}} l_{\mathrm{d}}],$$

$$D_2 = \frac{\rho}{1+\rho} T \frac{\lambda_{\mathrm{s}}}{K_{\mathrm{s}}^{\mathrm{ef}}} \sin[\lambda_{\mathrm{s}} l_{\mathrm{d}}]. \tag{37}$$

Similarly, for elastic fields: $0 \leqslant x \leqslant l_{\mathrm{e}}$ the condition $\tau_{\mathrm{l}}^{\mathrm{e}}(l_{\mathrm{e}}) = -\tau_{\mathrm{l}}^{\mathrm{C}}$ provides the constant C_1, thus

$$C_1 = -\frac{\tau_{\mathrm{l}}^{\mathrm{C}}}{K_{\mathrm{t}}^{\mathrm{ef}}} \frac{1}{\sinh[\lambda_{\mathrm{e}} l_{\mathrm{e}}]}. \tag{38}$$

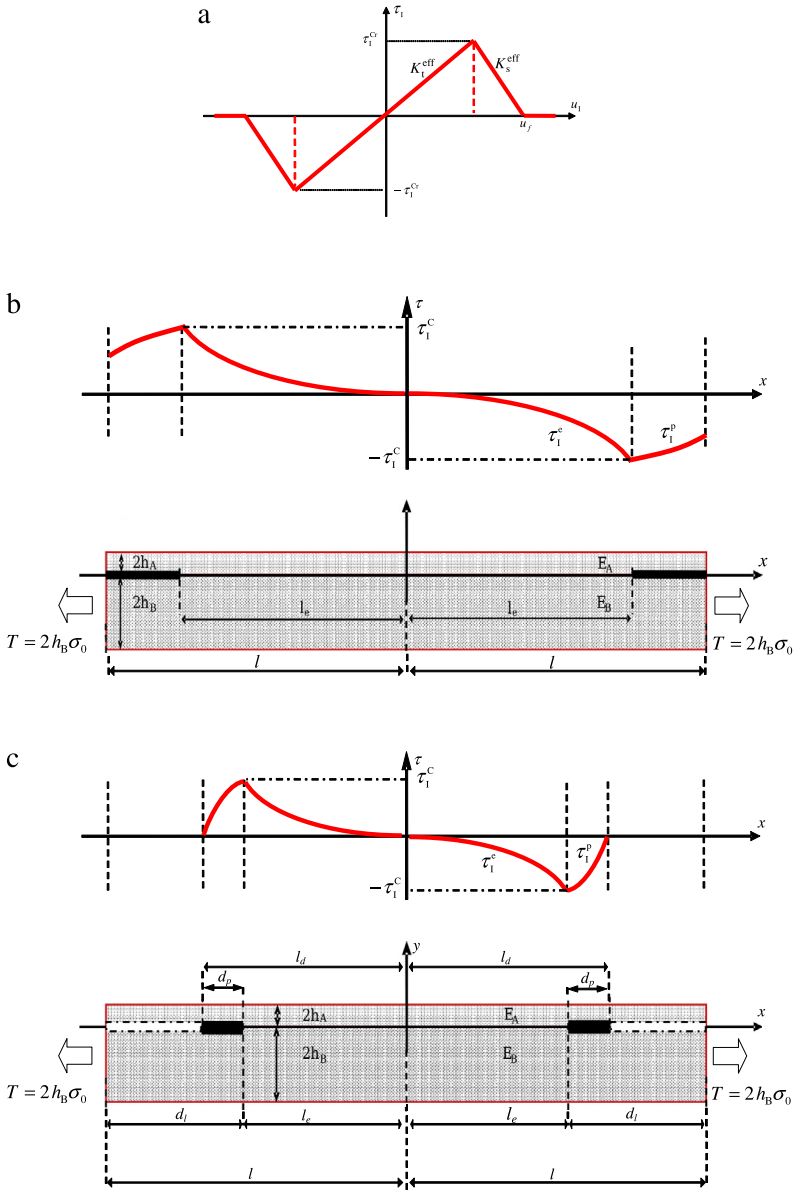

Fig. 6. Progressive growth of delamination: interface model (a); substrate mechanical loading and shear stress field for initial growth of damage zone, (b); growth of delamination and motion process zone, (c).

The mechanical fields are now expressed as follows in the elastic zone: $0 \leqslant x \leqslant l_e$:

$$\tau_I^e(x) = -\tau_I^C \frac{\sinh[\lambda_e x]}{\sinh[\lambda_e l_e]},$$
$$T_A^e(x) = -\frac{\tau_I^C}{\lambda_e}\frac{\cosh[\lambda_e x]}{\sinh[\lambda_e l_e]} + \frac{\rho}{1+\rho}T, \qquad (39)$$
$$T_B^e(x) = \frac{\tau_I^C}{\lambda_e}\frac{\cosh[\lambda_e x]}{\sinh[\lambda_e l_e]} + \frac{1}{1+\rho}T$$

in the damage zone: $l_e \leqslant x \leqslant l_d$:

$$\tau_I^p(x) = \frac{\rho}{1+\rho}T\lambda_s\big[\cos[\lambda_s l_d]\sin[\lambda_s x] - \sin[\lambda_s l_d]\cos[\lambda_s x]\big],$$
$$T_A^p(x) = \frac{\rho}{1+\rho}T\big[1 - \cos[\lambda_s l_d]\cos[\lambda_s x] - \sin[\lambda_s l_d]\sin[\lambda_s x]\big], \qquad (40)$$
$$T_B^p(x) = \frac{\rho}{1+\rho}T\Big[\frac{1}{\rho} + \cos[\lambda_s l_d]\cos[\lambda_s x] + \sin[\lambda_s l_d]\sin[\lambda_s x]\Big].$$

Requiring $\tau_I^p(l_e) = -\tau_I^C$ and continuity condition $[T_A] = 0$ at $x = l_e$, two equations specifying l_e and l_d are obtained

$$
\begin{aligned}
u_{\mathrm{B}}^{\mathrm{e}}(x) &= \frac{\lambda_{\mathrm{e}}^2 T(l)x + (1+\rho)\tau_{\mathrm{I}}^{\mathrm{C}} \sinh[\lambda_{\mathrm{e}}x]}{\sinh[\lambda_{\mathrm{e}}l_{\mathrm{e}}]2E_{\mathrm{B}}h_{\mathrm{B}}\lambda_{\mathrm{e}}^2(1+\rho)},\\
u_{\mathrm{B}}^{\mathrm{p}}(x) &= \frac{\lambda_{\mathrm{s}}(\tau_{\mathrm{I}}^{\mathrm{C}} + \rho\tau_{\mathrm{I}}^{\mathrm{C}} + \lambda_{\mathrm{e}}^2 T(l)x) + \lambda_{\mathrm{e}}^2\rho T(l)(\sin[\lambda_{\mathrm{s}}(l_{\mathrm{d}}-l_{\mathrm{e}})] - \sin[\lambda_{\mathrm{s}}(l_{\mathrm{d}}-x)])}{2E_{\mathrm{B}}h_{\mathrm{B}}\lambda_{\mathrm{e}}^2\lambda_{\mathrm{s}}(1+\rho)},\\
u_{\mathrm{B}}^{\mathrm{h}}(x) &= \frac{\lambda_{\mathrm{s}}((1+\rho)\tau_{\mathrm{I}}^{\mathrm{C}} + \lambda_{\mathrm{e}}^2 T(l)(-l_{\mathrm{d}}\rho + x + \rho x)) + \lambda_{\mathrm{e}}^2\rho T(l)\sin[\lambda_{\mathrm{s}}(l_{\mathrm{d}}-l_{\mathrm{e}})]}{2E_{\mathrm{B}}h_{\mathrm{B}}\lambda_{\mathrm{e}}^2\lambda_{\mathrm{s}}(1+\rho)}.
\end{aligned}
\tag{44}
$$

Box II.

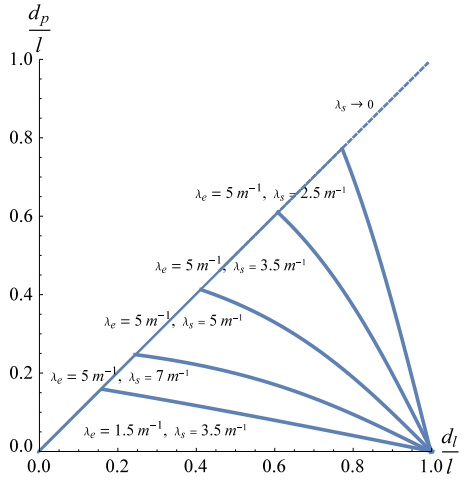

Fig. 7. Progression of damage zone length for elastic-softening model and varying parameters $\lambda_{\mathrm{e}}, \lambda_{\mathrm{s}}$ and for fixed parameters: $l = 0.3$ m, $h = 0.5 \cdot 10^{-3}$ m, $\tau_{\mathrm{I}}^{\mathrm{C}} = 2$ MPa.

$$
\begin{cases}
T = \dfrac{\rho+1}{\rho}\dfrac{\tau_{\mathrm{I}}^{\mathrm{C}}}{\lambda_{\mathrm{s}}}\dfrac{1}{\sin[\lambda_{\mathrm{s}}(l_{\mathrm{d}}-l_{\mathrm{e}})]} = \dfrac{\rho+1}{\rho}\dfrac{\tau_{\mathrm{I}}^{\mathrm{C}}}{\lambda_{\mathrm{s}}}\dfrac{1}{\sin[\lambda_{\mathrm{s}}d_{\mathrm{p}}]},\\
T\dfrac{\rho}{1+\rho}\cos[\lambda_{\mathrm{s}}d_{\mathrm{p}}] = \dfrac{\tau_{\mathrm{I}}^{\mathrm{C}}}{\lambda_{\mathrm{e}}}\coth[\lambda_{\mathrm{e}}l_{\mathrm{e}}].
\end{cases}
\tag{41}
$$

From (41) the following relation specifying the length of process zone, $d_{\mathrm{p}} = l_{\mathrm{d}} - l_{\mathrm{e}}$, is obtained

$$
d_{\mathrm{p}} = \frac{1}{\lambda_{\mathrm{s}}}\arctan\left[\frac{\lambda_{\mathrm{e}}}{\lambda_{\mathrm{s}}}\tanh[\lambda_{\mathrm{e}}l_{\mathrm{e}}]\right] \tag{42}
$$

and the relation between the load of plate B and the elastic zone length is

$$
T = \frac{\rho+1}{\rho}\frac{\tau_{\mathrm{I}}^{\mathrm{C}}}{\lambda_{\mathrm{s}}}\coth[\lambda_{\mathrm{e}}l_{\mathrm{e}}]\sqrt{1+\left(\frac{\lambda_{\mathrm{s}}}{\lambda_{\mathrm{e}}}\right)^2\tanh^2[\lambda_{\mathrm{e}}l_{\mathrm{e}}]}. \tag{43}
$$

The displacement field of plate B is expressed for elastic, process and delaminated zones. Satisfying the boundary conditions $u_{\mathrm{B}}^{\mathrm{e}}(0) = 0$ and continuity conditions $[u_{\mathrm{B}}(l_{\mathrm{e}})] = 0$ and $[u_{\mathrm{B}}(l_{\mathrm{d}})] = 0$, we have Eq. (44) in Box II

It is seen from (42) that the length d_{p} of the process zone decreases during the delamination process and vanishes for $l_{\mathrm{e}} \to 0$. On the other hand, the applied load expressed by (43) increases and tends to infinity for $l_{\mathrm{e}} \to 0$. This effect can easily be interpreted from the elastic solution and diagram in Fig. 5(c). In fact the required delamination load increases for short plate. Fig. 7 presents the progression of process zone length d_{p} versus total delamination affected portion of the interface d_{l}. Initially $d_{\mathrm{p}} = d_{\mathrm{l}}$ during the zone growth phase and next d_{p} decreases during the zone translation phase.

3.3. Specific case 1: elastic-perfectly brittle bond model: $K_{\mathrm{s}}^{\mathrm{eff}} = \infty$

The elastic–brittle bonding model is frequently used to specify the lower bound on the delamination load. Now the process zone does not exist as there is an abrupt transition from the elastic shear stress value $\tau_{\mathrm{I}}^{\mathrm{C}}$ to failure at fixed value of $u_{\mathrm{I}} = u_{\mathrm{If}}$, Fig. 8. Following (25), we have for $0 \leqslant x \leqslant l_{\mathrm{e}}$:

$$
\begin{aligned}
u_{\mathrm{I}}^{\mathrm{e}}(x) &= -\frac{\rho}{1+\rho}T\frac{\lambda_{\mathrm{e}}}{K_{\mathrm{t}}^{\mathrm{ef}}}\frac{\sinh[\lambda_{\mathrm{e}}x]}{\cosh[\lambda_{\mathrm{e}}l_{\mathrm{e}}]},\\
\tau_{\mathrm{I}}^{\mathrm{e}}(x) &= -\frac{\rho}{1+\rho}T\lambda_{\mathrm{e}}\frac{\sinh[\lambda_{\mathrm{e}}x]}{\cosh[\lambda_{\mathrm{e}}l_{\mathrm{e}}]},\\
T_{\mathrm{A}}^{\mathrm{e}}(x) &= \frac{\rho}{1+\rho}T\left(1-\frac{\cosh[\lambda_{\mathrm{e}}x]}{\cosh[\lambda_{\mathrm{e}}l_{\mathrm{e}}]}\right),\\
T_{\mathrm{B}}^{\mathrm{e}}(x) &= \frac{1}{1+\rho}T\left(1+\rho\frac{\cosh[\lambda_{\mathrm{e}}x]}{\cosh[\lambda_{\mathrm{e}}l_{\mathrm{e}}]}\right),
\end{aligned}
\tag{45}
$$

for $l_{\mathrm{e}} \leqslant x \leqslant l$:

$$
\tau_{\mathrm{I}}(x) = 0, \qquad T_{\mathrm{A}}(x) = 0, \qquad T_{\mathrm{B}}(x) = T. \tag{46}
$$

Setting $\tau_{\mathrm{I}}^{\mathrm{e}}(l_{\mathrm{e}}) = -\tau_{\mathrm{I}}^{\mathrm{C}}$, it is obtained

$$
\begin{aligned}
T^{\mathrm{C}} &= \frac{1+\rho}{\rho}\frac{\tau_{\mathrm{I}}^{\mathrm{C}}}{\lambda_{\mathrm{e}}}\coth[\lambda_{\mathrm{e}}l_{\mathrm{e}}]\\
&= \frac{1+\rho}{\rho}\frac{\tau_{\mathrm{I}}^{\mathrm{C}}}{\lambda_{\mathrm{e}}}\coth[\lambda_{\mathrm{e}}(l-d_{\mathrm{I}})]
\end{aligned}
\tag{47}
$$

and the displacement for the boundary condition $u_{\mathrm{B}}(0) = 0$ is $0 \leqslant x \leqslant l_{\mathrm{e}}$:

$$
\begin{aligned}
u_{\mathrm{A}}^{\mathrm{e}}(x) &= \frac{\rho}{1+\rho}\frac{T}{2h_{\mathrm{A}}E_{\mathrm{A}}}\left(x-\frac{1}{\lambda_{\mathrm{e}}}\frac{\sinh[\lambda_{\mathrm{e}}x]}{\cosh[\lambda_{\mathrm{e}}l_{\mathrm{e}}]}\right)\\
u_{\mathrm{B}}^{\mathrm{e}}(x) &= \frac{1}{1+\rho}\frac{T}{2h_{\mathrm{B}}E_{\mathrm{B}}}\left(x+\frac{\rho}{\lambda_{\mathrm{e}}}\frac{\sinh[\lambda_{\mathrm{e}}x]}{\cosh[\lambda_{\mathrm{e}}l_{\mathrm{e}}]}\right)
\end{aligned}
\tag{48}
$$

and it is noted that $u_{\mathrm{A,B}}^{\mathrm{h}}(l_{\mathrm{e}}) = u_{\mathrm{A,B}}^{\mathrm{e}}(l_{\mathrm{e}})$ for $l_{\mathrm{e}} \leqslant x \leqslant l$:

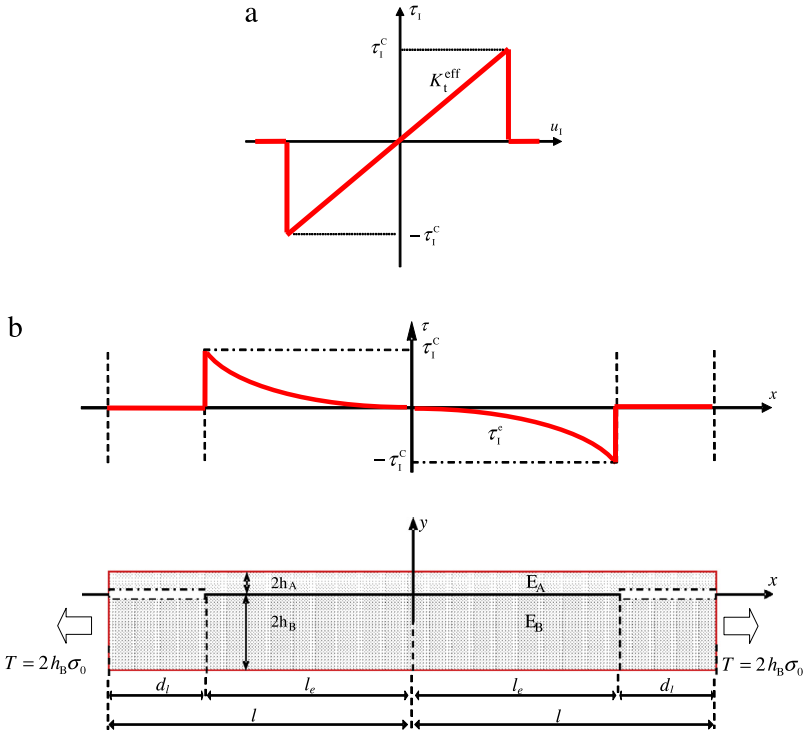

Fig. 8. Elastic–brittle interface model (a); shear stress field for growth of delamination in bi-layer system, (b).

$$u_{\rm A}^{\rm h}(x) = \frac{\rho}{1+\rho}\frac{T}{2h_{\rm A}E_{\rm A}}\left(l_{\rm e} - \frac{1}{\lambda_{\rm e}}\tanh[\lambda_{\rm e}l_{\rm e}]\right)$$
$$u_{\rm B}^{\rm h}(x) = \frac{1}{1+\rho}\frac{T}{2h_{\rm B}E_{\rm B}}\left(l_{\rm e} + \frac{\rho}{\lambda_{\rm e}}\tanh[\lambda_{\rm e}l_{\rm e}]\right) + \frac{T}{2h_{\rm B}E_{\rm B}}(x - l_{\rm e}). \tag{49}$$

It is seen that the load T increases with the length of delaminated zone $d_{\rm I}$. The formula (47) is identical to (27) expressing the load value at the onset of delamination.

3.4. Specific case 2: elastic-perfectly plastic bond model: $K_{\rm s}^{\rm eff} = 0$

Referring to the previous case, the growth of plastic zones from the plate ends induces higher load values in order to drive the delamination process, Fig. 9, namely

$$T^{\rm C} = \frac{1+\rho}{\rho}\tau_{\rm I}^{\rm C}\left[\frac{1}{\lambda_{\rm e}}\coth[\lambda_{\rm e}(l-d_{\rm I})] + d_{\rm I}\right] \tag{50}$$

and the displacement at the end of plate B is

$$u_{\rm B}^{\rm p}(x) = u_{\rm B}^{\rm e}(l_{\rm e}) - \frac{(l-x)(2T + \tau_{\rm I}^{\rm C}(x - 2l + l_{\rm e}))}{4E_{\rm B}h_{\rm B}}, \tag{51}$$

where

$$u_{\rm B}^{\rm e}(l_{\rm e}) = l_{\rm e}\frac{1}{1+\rho}\frac{T}{2E_{\rm B}h_{\rm B}} + \frac{\tanh[\lambda_{\rm e}l_{\rm e}]}{2E_{\rm B}h_{\rm B}\lambda_{\rm e}} \times\left[\frac{\rho}{1+\rho}T - \tau_{\rm I}^{\rm C}(l - l_{\rm e})\right]. \tag{52}$$

3.5. Specific case 3: rigid-softening interface layer: $\lambda_{\rm e} \to \infty$

The analysis presented for the elastic-softening response can be particularized for several specific cases requiring more detailed discussion. Consider first the case when the elastic modulus $K_{\rm t}^{\rm eff}$ tends to infinity and the rigid-softening response occurs. This modulus is difficult to identify for the FEM analysis where high values are usually assumed. The softening rule is now expressed as follows

$$\tau_{\rm I} = \tau_{\rm I}^{\rm C} - K_{\rm s}^{\rm ef}u_{\rm I}, \quad G_{\rm If} = \frac{1}{2}\tau_{\rm I}^{\rm C}u_{\rm If} = \frac{1}{2}\frac{(\tau_{\rm I}^{\rm C})^2}{K_{\rm s}^{\rm ef}}. \tag{53}$$

As $u_{\rm I} = 0$ for $|\tau_{\rm I}| < \tau_{\rm I}^{\rm C}$, then only homogeneous stress states are allowed for which $\tau_{\rm I} = u_{\rm I} = 0$. After load application the damage process zones are formed near the plates ends and in the central part the homogeneous stress state is generated, Fig. 10.

From the equilibrium equations for the damage growth phase

$$\frac{{\rm d}T_{\rm A}}{{\rm d}x} = 2h_{\rm A}E_{\rm A}\frac{{\rm d}^2u_{\rm A}}{{\rm d}x^2} = -\tau_{\rm I}^{\rm C} - K_{\rm s}^{\rm ef}u_{\rm I}$$
$$\frac{{\rm d}T_{\rm B}}{{\rm d}x} = 2h_{\rm B}E_{\rm B}\frac{{\rm d}^2u_{\rm B}}{{\rm d}x^2} = \tau_{\rm I}^{\rm C} + K_{\rm s}^{\rm ef}u_{\rm I}. \tag{54}$$

The following differential equation is obtained

$$\frac{{\rm d}^2u_{\rm I}}{{\rm d}x^2} + \lambda_{\rm s}^2u_{\rm I} = -\left(\frac{1}{2h_{\rm A}E_{\rm A}} + \frac{1}{2h_{\rm B}E_{\rm B}}\right)\tau_{\rm I}^{\rm C} \tag{55}$$

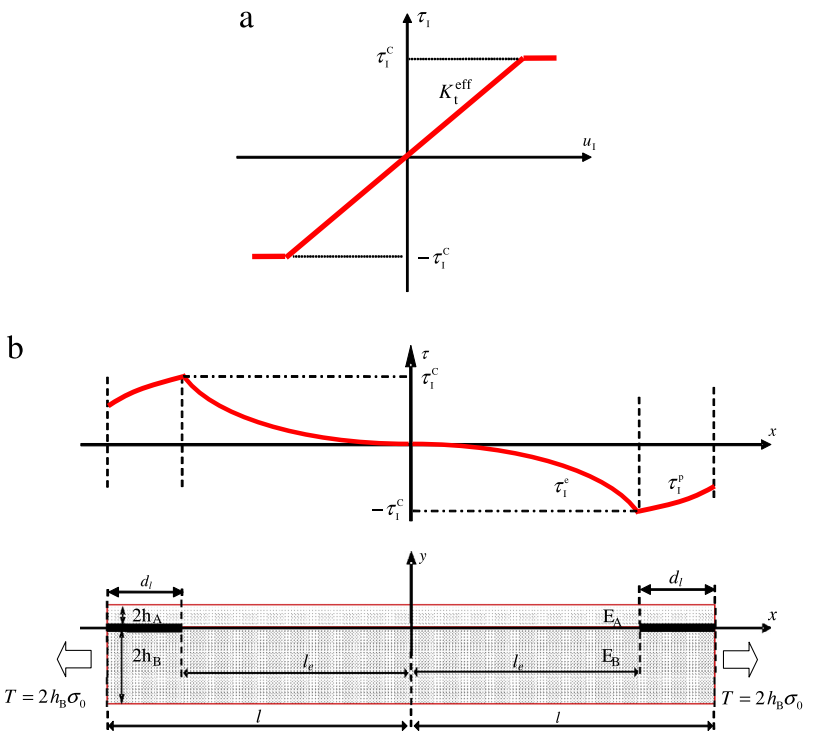

Fig. 9. Elastic-perfectly plastic interface model (a); substrate mechanical loading and shear stress field for motion of damage zone (b).

where

$$\lambda_{\rm s}^2 = K_{\rm s}^{\rm ef}\left(\frac{1}{2h_{\rm A}E_{\rm A}} + \frac{1}{2h_{\rm B}E_{\rm B}}\right) = K_{\rm s}^{\rm ef}C_l \quad \text{and}$$
$$K_{\rm s}^{\rm ef} = \frac{(\tau_{\rm I}^{\rm C})^2}{2G_{\rm If}} \tag{56}$$

where, C_l denotes the elastic layer compliance, expressed by the bracketed term of (56). Satisfying the continuity conditions $[u_{\rm I}] = [u_{\rm I}'] = 0$ for $x = l_{\rm e}$ and the boundary conditions $T_{\rm A}(l) = 0$ it is obtained

$$\begin{aligned}
u_{\rm I}^{\rm p}(x) &= -\frac{\tau_{\rm I}^{\rm C}}{K_{\rm s}^{\rm ef}}(1 - \cos[\lambda_{\rm s}(x - l_{\rm e})])\\
\tau_{\rm I}^{\rm p}(x) &= -\tau_{\rm I}^{\rm C}\cos[\lambda_{\rm s}(x - l_{\rm e})]\\
T_{\rm A}^{\rm p}(x) &= \frac{\tau_{\rm I}^{\rm C}}{\lambda_{\rm s}}(\sin[\lambda_{\rm s}d] - \sin[\lambda_{\rm s}(x - l_{\rm e})])\\
T_{\rm B}^{\rm p}(x) &= T - \frac{\tau_{\rm I}^{\rm C}}{\lambda_{\rm s}}(\sin[\lambda_{\rm s}d] - \sin[\lambda_{\rm s}(x - l_{\rm e})])
\end{aligned} \tag{57}$$

where, $d = l - l_{\rm e}$. For $x = l_{\rm e}$, the values of $T_{\rm A}$ and $T_{\rm B}$ should be equal to the homogeneous state values, thus

$$\begin{aligned}
T_{\rm A} &= \frac{\tau_{\rm I}^{\rm C}}{\lambda_{\rm s}}\sin[\lambda_{\rm s}d] = \frac{\rho}{1+\rho}T,\\
\sin[\lambda_{\rm s}d] &= \frac{\lambda_{\rm s}}{\tau_{\rm I}^{\rm C}}\frac{\rho}{1+\rho}T
\end{aligned} \tag{58}$$

and the homogeneous stress state occurs for $-l_{\rm e} \le x \le l_{\rm e}$.

The end of growth phase takes place when $\tau_{\rm I}^{\rm p}(l) = 0$, thus

$$-\tau_{\rm I}^{\rm C}\cos[\lambda_{\rm s}d_f] = 0, \quad \lambda_{\rm s}d_f = \frac{\pi}{2} \text{ and } d_f = \frac{\pi}{2}\frac{1}{\lambda_{\rm s}}. \tag{59}$$

It is seen that at the end of growth process the length of the process zone reaches its critical value d_f expressed by (59). Alternatively, it can also be presented in the form

$$d_f = \frac{\pi}{2}K_{\rm s}\frac{1}{\tau_{\rm I}^{\rm C}} = \sqrt{\frac{2G_{\rm If}}{C_l}}. \tag{60}$$

The critical value d_f depends on three parameters, with the most sensitive dependence on $\tau_{\rm I}^{\rm C}$ and less sensitive dependence on $G_{\rm If}$ and C_l.

The progression phase of the process zone proceeds at the constant load

$$T = \frac{1+\rho}{\rho}\frac{\tau_{\rm I}^{\rm C}}{\lambda_{\rm s}} \tag{61}$$

and the increasing displacement $u_{\rm B}(l)$, Fig. 10(b). We have

$$\begin{aligned}
&l_{\rm p} \leqslant x \leqslant l : \tau_{\rm I} = 0, \qquad T_{\rm A} = 0,\\
&T_{\rm B} = T = \frac{\tau_{\rm I}^{\rm C}}{\lambda_{\rm s}^{\rm eff}}\frac{1+\rho}{\rho},\\
&l_{\rm e} \leqslant x \leqslant l_{\rm p} : \tau_{\rm I}^{\rm p}(x) = -\tau_{\rm I}^{\rm C}\cos[\lambda_{\rm s}(x - l_{\rm e})],\\
&T_{\rm A}^{\rm p}(x) = \frac{\tau_{\rm I}^{\rm C}}{\lambda_{\rm s}}(1 - \sin[\lambda_{\rm s}(x - l_{\rm p})]),\\
&0 \leqslant x \leqslant l_{\rm e} : T_{\rm A} = T\frac{\rho}{1+\rho} = \frac{\tau_{\rm I}^{\rm C}}{\lambda_{\rm s}}, \qquad T_{\rm B} = \frac{\tau_{\rm I}^{\rm C}}{\lambda_{\rm s}}\frac{1}{1+\rho}.
\end{aligned} \tag{62}$$

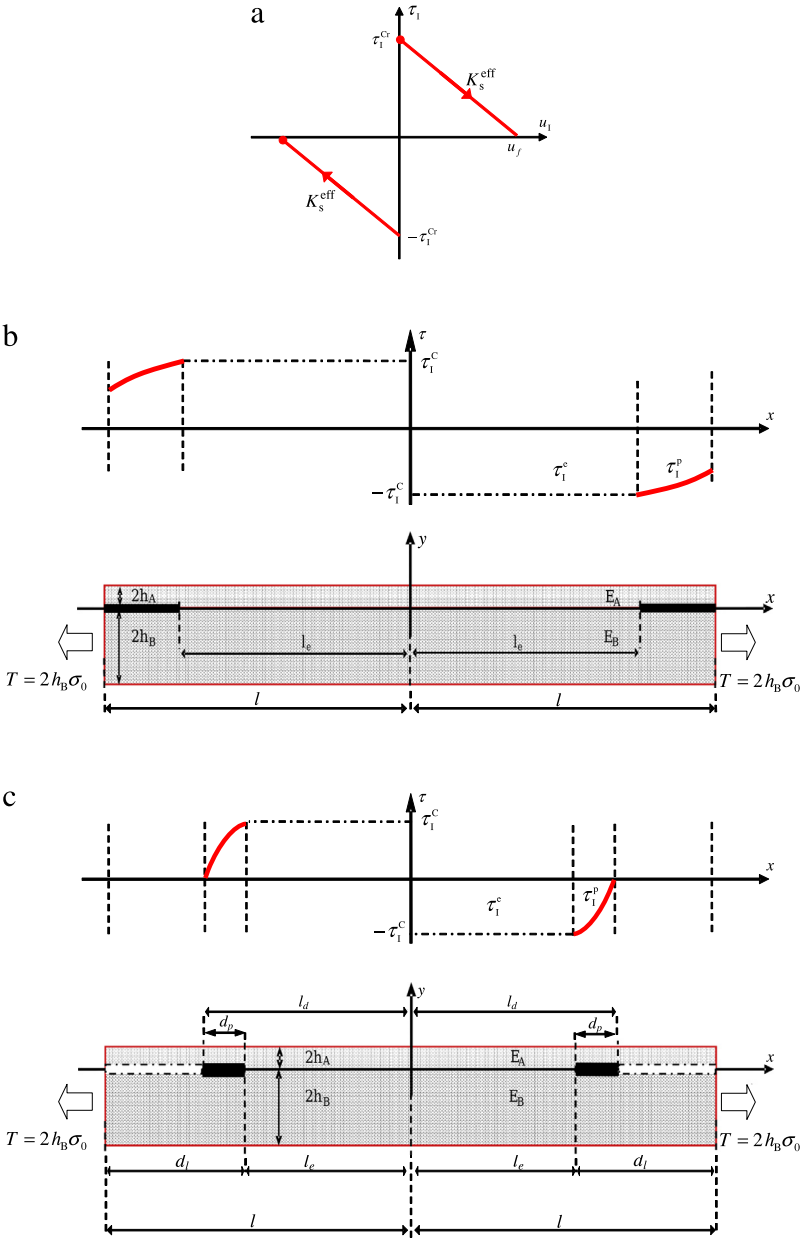

Fig. 10. Rigid-softening interface model, (a); process zone growth, (b); propagation, (c).

The progression phase is determined when the damage process zones reach the symmetry axes at $x = 0$, Fig. 11. The final phase, named *the degradation of process zone* next proceeds. Assume u_1 to vary discontinuously at $x = 0$ with growing value u_1, at constant process zone length d_f, so that

$$u_1 = -\frac{\tau_1^C - K_s^{ef} u_1}{K_s^{ef}}(1 - \cos[\lambda_s x]),$$
$$\tau_1 = -(\tau_1^C - K_s^{ef} u_1)\cos[\lambda_s x], \tag{63}$$
$$T = \frac{\tau_1^C - K_s^{ef} u_1}{\lambda_s}(1 - \sin[\lambda_s x]), \qquad T_B = T - T_A.$$

Final degradation occurs when $K_s^{ef} u_1 = \tau_1^C$, and $T_A = 0$, $T_B = T$. It is seen that for the rigid-softening model, the process of full delamination proceeds differently from that for elastic-softening model of bonding interface, where the continuing reduction of length of the process zone occurred at increasing plate loading.

Fig. 12 presents the dependence of the applied load T or the length of delaminated zone. It is seen that for increasing value of λ_e, the $T - d_l$ diagram tends to that predicted by the rigid-softening model. Fig. 13 presents the $T - u_B(l)$ diagrams for several cases analyzed in the paper.

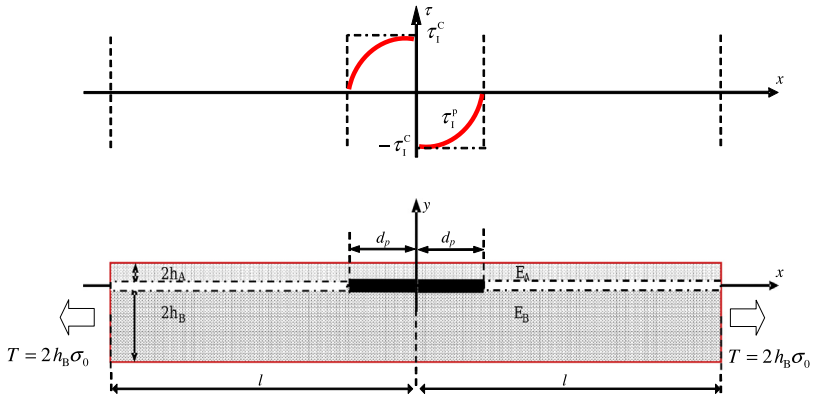

Fig. 11. Degradation of the process zone.

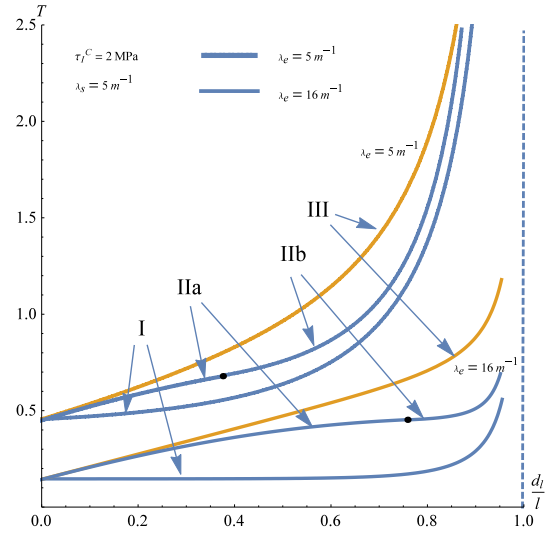

Fig. 12. Relation of the driving force $T(l)$ to the delamination zone d_I, for parameters: $l = 0.3$ m, $\rho = 11$, $\lambda_s = 5\ \mathrm{m}^{-1}$, $h = 0.5 \cdot 10^{-3}$ m, $\tau_I^C = 2$ MPa and two values of λ_e. Here I describes brittle interface response, IIa plastic softening behavior until delamination occurs, IIb full delamination with damage process zone, III—perfectly plastic behavior.

4. Lap-joint analysis

4.1. Elastic analysis

Consider the lap joint shown in Fig. 14 with the plate B attached to a fixed support at $x = 0$ and plate A axially loaded at its end $x = l$ by the force T and with the free end at $x = 0$. The reference system x, y is now put at the left plate end. Applying the elastic solution (12) with the boundary conditions $T_A(l) = T$, $T_A(0) = 0$, the static field can be determined.

From (12) it follows that

$$T(x) = T_A(x) + T_B(x) = C_3 2h_A\left(1 + \frac{h_B E_B}{h_A E_A}\right) = C_3 2h_A\left(1 + \frac{1}{\rho}\right) \tag{64}$$

and

$$2h_A C_3 = \frac{\rho}{1+\rho}T(l).$$

Satisfying the boundary conditions, the following formulae are obtained

$$\begin{aligned}
\tau_I &= \lambda_e \frac{T}{1+\rho}\frac{\rho\cosh[\lambda_e(l-x)] + \cosh[\lambda_e x]}{\sinh[\lambda_e l]},\\
T_A &= \frac{T}{1+\rho}\frac{\rho\sinh[\lambda_e l] - \sinh[\lambda_e(l-x)] + \sinh[\lambda_e x]}{\sinh[\lambda_e l]},\\
T_B &= \frac{T}{1+\rho}\frac{\sinh[\lambda_e l] - \sinh[\lambda_e x] + \rho\sinh[\lambda_e(l-x)]}{\sinh[\lambda_e l]}.
\end{aligned} \tag{65}$$

The stress τ_I at the plate ends $x = 0$ and $x = l$ is

$$\begin{aligned}
\tau_I(l) &= \frac{\lambda_e}{1+\rho}T\frac{\rho + \cosh[\lambda_e l]}{\sinh[\lambda_e l]},\\
\tau_I(0) &= \frac{\lambda_e}{1+\rho}T\frac{\rho\cosh[\lambda_e l] + 1}{\sinh[\lambda_e l]}
\end{aligned} \tag{66}$$

and

$$\frac{\tau_I(0)}{\tau_I(l)} = \frac{1 + \rho\cosh[\lambda_e l]}{\rho + \cosh[\lambda_e l]}. \tag{67}$$

It is seen in view of the inequality $\cosh[\lambda_e l] > 1$, that

$$\begin{aligned}
&\text{for} \quad \rho < 1 \qquad \tau_I(l) > \tau_I(0),\\
&\text{for} \quad \rho = 1 \qquad \tau_I(l) = \tau_I(0),\\
&\text{for} \quad \rho > 1 \qquad \tau_I(l) < \tau_I(0).
\end{aligned} \tag{68}$$

Fig. 15 presents the distribution of the shear stress $\tau_I(x)$ and of the forces $T_{A,B}(x)$ for different values of λ_e. It is seen that, similarly as in the previous case, for the increasing values of λ_e, the shear stress in the end zones increases and the force distribution tends to its homogeneous state in the central point portion. The critical load value at the onset of damage process now is specified as follows

$$\begin{aligned}
&\text{for} \quad \rho < 1 \qquad \tau_I(l) = \tau_I^C,\\
&T^C = \frac{\tau_I^C}{\lambda_e}(1+\rho)\frac{\sinh[\lambda_e l]}{\rho + \cosh[\lambda_e l]},\\
&\text{for} \quad \rho > 1 \qquad \tau_I(0) = \tau_I^C,\\
&T^C = \frac{\tau_I^C}{\lambda_e}(1+\rho)\frac{\sinh[\lambda_e l]}{1 + \rho\cosh[\lambda_e l]}
\end{aligned} \tag{69}$$

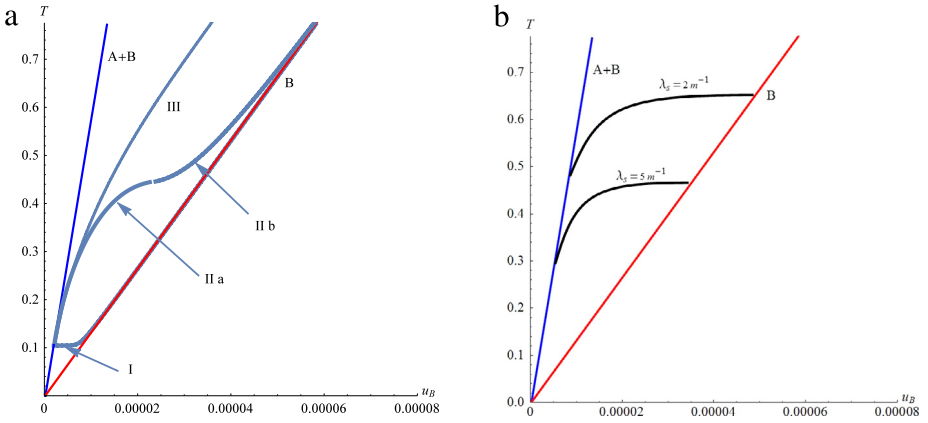

Fig. 13. (a) Load–displacement response of the bi-layer structure for elastic-softening model and parameters: $l = 0.3$ m, $\rho = 11$, $\lambda_e = 21 \cdot \mathrm{m}^{-1}$, $\lambda_s = 5\ \mathrm{m}^{-1}$, $h = 0.5 \cdot 10^{-3}$ m, $\tau_I^C = 2$ MPa. Here A+B indicates elastic solution for joined plates, B indicates elastic response for plate B only, I presents brittle interface response, IIa and IIb delamination with damage zone, III—perfectly plastic behavior; (b) Load–displacement diagrams for rigid-softening model.

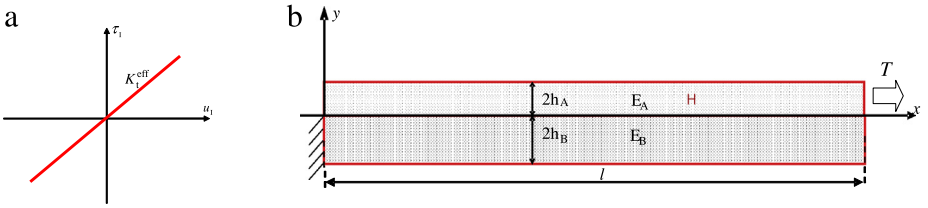

Fig. 14. The interface model (a), and lap-joint mechanical loading (b).

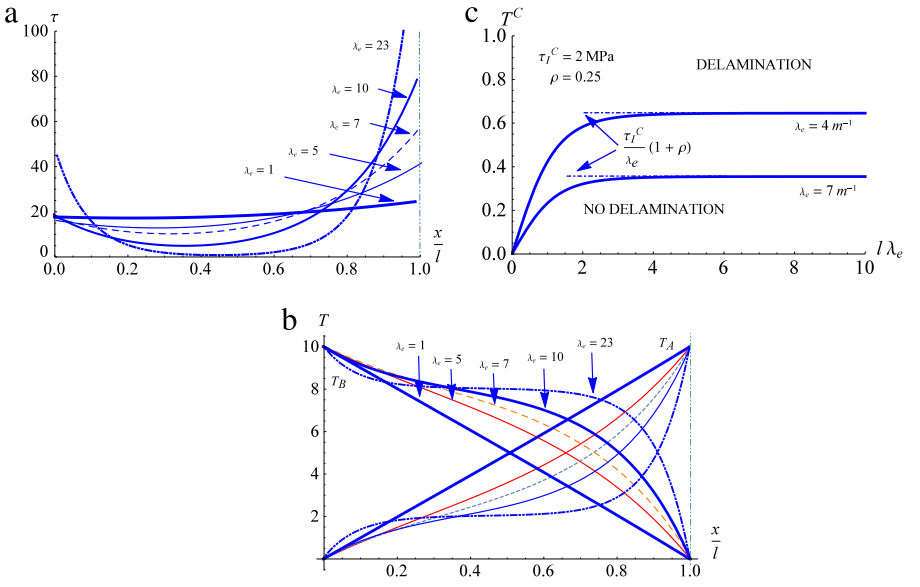

Fig. 15. Elastic distributions of the shear stress $\tau_I(x)$, (a) the forces $T_A(x)$, $T_B(x)$, (b) the critical force initiating the delamination process versus length of specimen l for different values of λ_e, (c).

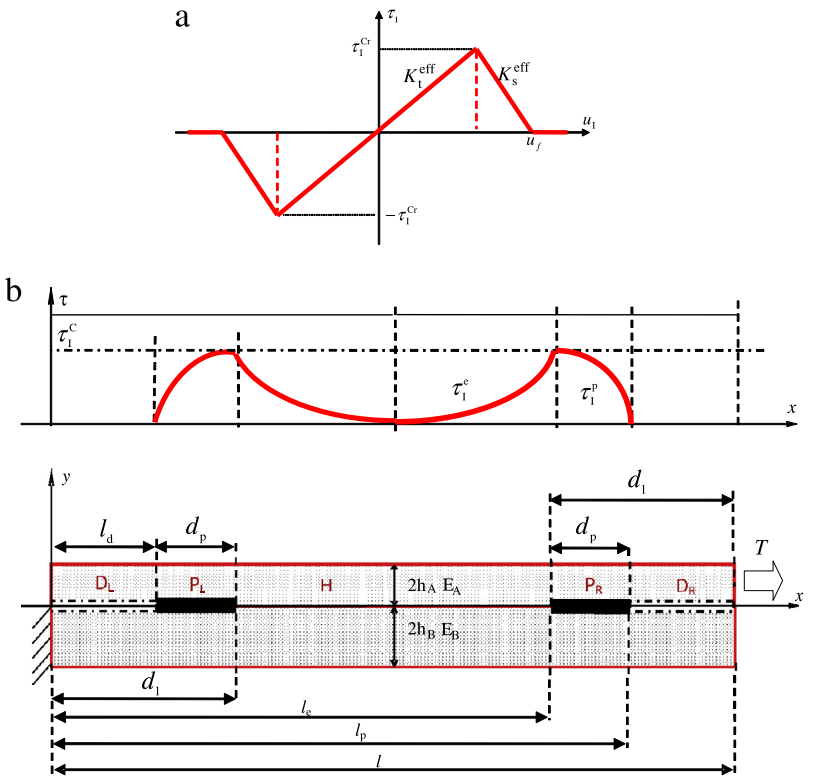

Fig. 16. The interface model, (a); delamination growth in the lap-joint mechanical loading for $\rho = 1$, (b).

and for $l \to \infty$ the critical load tends to $T_{\mathrm{l}}^{\mathrm{C}} = \frac{\tau_{\mathrm{l}}^{\mathrm{C}}}{\lambda_{\mathrm{e}}}(1+\rho)$ for $\rho < 1$ or $T_{\mathrm{l}}^{\mathrm{C}} = \frac{\tau_{\mathrm{l}}^{\mathrm{C}}}{\lambda_{\mathrm{e}}}\frac{1+\rho}{\rho}$ for $\rho > 1$.

4.2. Damage growth analysis for $\rho = 1$

For simplicity let us consider the case of symmetric delamination of lap joint for $\rho = 1$. As in the previous case, there are consecutive stages of delamination process, namely damage zone growth, delamination combined with motion of damage zone and finally degradation of damage zone. As for $\rho = 1$, there is symmetric distribution of the shear stress τ_{l} relative to the central axis, it is sufficient to provide the solution for $0 \le x \le l/2$ and next to extend it by applying the symmetry condition $\tau_{\mathrm{l}}(x) = \tau_{\mathrm{l}}(l-x)$.

4.2.1. Damage zone growth

The critical load value at the onset of damage growth is now specified by (69), thus

$$T^{\mathrm{C}} = \frac{2\tau_{\mathrm{l}}^{\mathrm{C}}}{\lambda_{\mathrm{e}}}\frac{\sinh[\lambda_{\mathrm{e}} l]}{1+\cosh[\lambda_{\mathrm{e}} l]} = \frac{2\tau_{\mathrm{l}}^{\mathrm{C}}}{\lambda_{\mathrm{e}}}\tanh\left[\lambda_{\mathrm{e}}\frac{l}{2}\right]. \tag{70}$$

Assume that for the elastic shear stress $\tau_{\mathrm{l}}(x) > \tau_{\mathrm{l}}^{\mathrm{C}}$ two damage process zones grow from both ends. Considering the growth process at the left end, assume existence of the damage zone of length d_{l} and the elastic zone in the central portion. From (19) the stress state is obtained in the segment for $0 \le x \le d_{\mathrm{l}}$ after satisfying the conditions $T_{\mathrm{A}} = 0$ for $x = 0$ and $\tau_{\mathrm{l}} = \tau_{\mathrm{l}}^{\mathrm{C}}$ for $x = d_{\mathrm{l}}$:

$$\begin{aligned}\tau_{\mathrm{l}}^{\mathrm{p}}(x) &= -\lambda_{\mathrm{s}}\frac{T}{2}\frac{\sin[\lambda_{\mathrm{s}}(d_{\mathrm{l}}-x)]}{\cos[\lambda_{\mathrm{s}} d_{\mathrm{l}}]} + \tau_{\mathrm{l}}^{\mathrm{C}}\frac{\cos[\lambda_{\mathrm{s}} x]}{\cos[\lambda_{\mathrm{s}} d_{\mathrm{l}}]},\\ T_{\mathrm{A}}^{\mathrm{p}}(x) &= \frac{T}{2}\left(1 - \frac{\cos[\lambda_{\mathrm{s}}(d_{\mathrm{l}}-x)]}{\cos[\lambda_{\mathrm{s}} d_{\mathrm{l}}]}\right) + \frac{\tau_{\mathrm{l}}^{\mathrm{C}}}{\lambda_{\mathrm{s}}}\frac{\sin[\lambda_{\mathrm{s}} x]}{\cos[\lambda_{\mathrm{s}} d_{\mathrm{l}}]}.\end{aligned} \tag{71}$$

The elastic state for $d_{\mathrm{l}} \le x \le l/2$ is determined from the relations (12) after satisfying the conditions $\tau_{\mathrm{l}}^{\mathrm{p}}(d_{\mathrm{l}}) = \tau_{\mathrm{l}}^{\mathrm{C}}$ and $\tau_{\mathrm{l}}'^{\mathrm{p}}(l/2) = 0$. It is obtained

$$\begin{aligned}\tau_{\mathrm{l}}^{\mathrm{p}}(x) &= \tau_{\mathrm{l}}^{\mathrm{C}}\frac{\cosh[\lambda_{\mathrm{e}}(l/2-x)]}{\cosh[\lambda_{\mathrm{e}}(l/2-d_{\mathrm{l}})]},\\ T_{\mathrm{A}}^{\mathrm{p}}(x) &= \frac{T}{2} - \frac{\tau_{\mathrm{l}}^{\mathrm{C}}}{\lambda_{\mathrm{e}}}\frac{\sinh[\lambda_{\mathrm{e}}(l/2-x)]}{\cosh[\lambda_{\mathrm{e}}(l/2-d_{\mathrm{l}})]}.\end{aligned} \tag{72}$$

From the condition of continuity of T_{A} for $x = d_{\mathrm{l}}$, the relation specifying the length of damage zone is obtained, thus

$$\frac{T}{2}\frac{1}{\cos[\lambda_{\mathrm{s}} d_{\mathrm{l}}]} = \frac{\tau_{\mathrm{l}}^{\mathrm{C}}}{\lambda_{\mathrm{s}}}\tan[\lambda_{\mathrm{s}} d_{\mathrm{l}}] + \frac{\tau_{\mathrm{l}}^{\mathrm{C}}}{\lambda_{\mathrm{e}}}\tanh[\lambda_{\mathrm{e}}(l/2-d_{\mathrm{l}})]. \tag{73}$$

Let us note that for $d_{\mathrm{l}} = 0$ the critical load value (70) is obtained from (72). The full delamination process starts when $\tau_{\mathrm{l}}^{\mathrm{p}}(0) = 0$, and from (71), (72) the required load

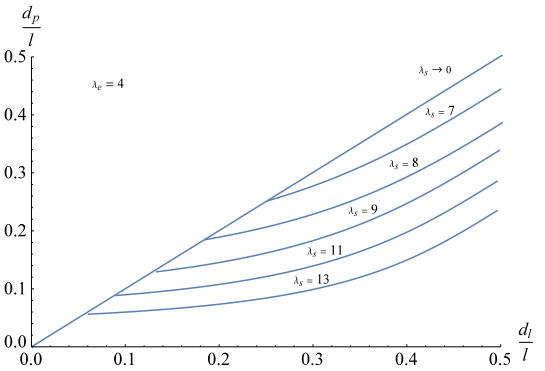

Fig. 17. Progression of damage zone length for different elastic–plastic softening values and $l = 0.5$ m, $h = 0.5 \cdot 10^{-3}$ m, $\tau_{\mathrm{l}}^{\mathrm{C}} = 1$ MPa. Lap-joint structure.

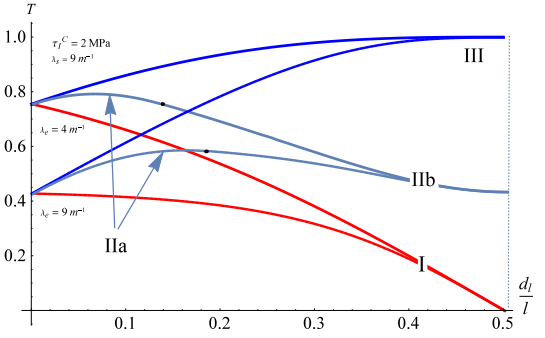

Fig. 18. Evolution of the driving force T to increase the delamination zone d_{l}. For fixed parameters: $l = 0.5$ m, $\rho = 1, \lambda_{\mathrm{s}} = 9 \cdot \mathrm{m}^{-1}, h = 0.5 \cdot 10^{-3}$ m, $\tau_{\mathrm{l}}^{\mathrm{C}} = 2$ MPa and two values of λ_{e}. Here I describes brittle interface response, IIa plastic softening behavior until delamination occurs, IIb delamination with growing damage zone, III—elastic-perfectly plastic model.

value and the damage zone length are obtained

$$T^{\mathrm{D}} = \frac{2\tau_{\mathrm{l}}^{\mathrm{C}}}{\lambda_s \sin[\lambda_s d_p]},$$
$$\tan[\lambda_s d_{\mathrm{l}}] \tanh\left[\lambda_e \left(\frac{l}{2} - d_{\mathrm{l}}\right)\right] = \frac{\lambda_e}{\lambda_s}. \tag{74}$$

4.2.2. Delamination growth

Referring to Fig. 16, the delamination portion length is denoted by l_{d} and the total damaged length by d_{l}, with the damaged process zone of length d_{p}. Now the conditions: $\tau_{\mathrm{l}}(l_{\mathrm{d}}) = 0$, $\tau_{\mathrm{l}}(d_{\mathrm{l}}) = \tau_{\mathrm{l}}^{\mathrm{C}}$ and $T_{\mathrm{A}}(d_{\mathrm{l}}) = 0$ are applied, and for $l_{\mathrm{d}} \le x \le d_{\mathrm{l}}$ we have

$$\tau_{\mathrm{l}}(x) = \tau_{\mathrm{l}}^{\mathrm{C}} \frac{\sin[\lambda_{\mathrm{s}}(x - l_{\mathrm{d}})]}{\sin[\lambda_{\mathrm{s}} d_{\mathrm{p}}]},$$
$$T_{\mathrm{A}}(x) = \frac{T}{2} - \frac{\tau_{\mathrm{l}}^{\mathrm{C}}}{\lambda_{\mathrm{s}}} \frac{\cos[\lambda_{\mathrm{s}}(x - l_{\mathrm{d}})]}{\sin[\lambda_{\mathrm{s}} d_{\mathrm{p}}]}. \tag{75}$$

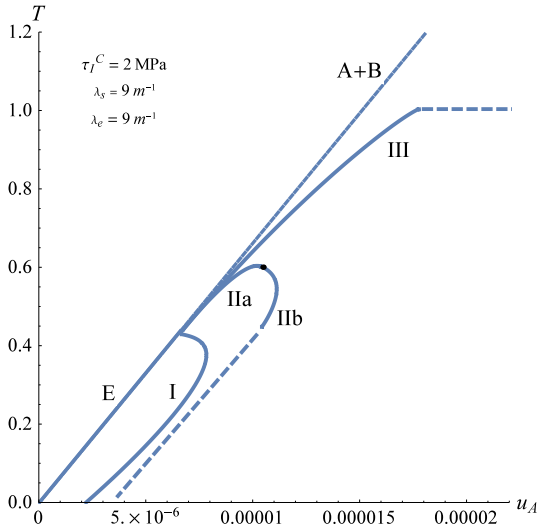

Fig. 19. Example of load–displacement response of the lap-joint structure affected by the continuous delamination process for parameters: $l = 0.5$ m, $\rho = 1$, $\lambda_{\mathrm{e}} = 9 \cdot \mathrm{m}^{-1}$, $\lambda_{\mathrm{s}} = 9 \cdot \mathrm{m}^{-1}$, $h = 0.5 \cdot 10^{-3}$ m, $\tau_{\mathrm{l}}^{\mathrm{C}} = 2$ MPa. Here A+B indicates elastic solution for joined plates, E indicates elastic response for initial loading, I presents brittle interface response, IIa and IIb delamination with damage zone, III—elastic-perfectly plastic response.

In the elastic zone $d_{\mathrm{l}} \le x \le l/2$ the stress state is presented as follows

$$\tau_{\mathrm{l}}(x) = \tau_{\mathrm{l}}^{\mathrm{C}} \frac{\cosh[\lambda_{\mathrm{e}}(l/2 - x)]}{\cosh[\lambda_{\mathrm{e}}(l/2 - d_{\mathrm{l}})]},$$
$$T_{\mathrm{A}}(x) = \frac{T}{2} - \frac{\tau_{\mathrm{l}}^{\mathrm{C}}}{\lambda_{\mathrm{e}}} \frac{\sinh[\lambda_{\mathrm{e}}(l/2 - x)]}{\cosh[\lambda_{\mathrm{e}}(l/2 - d_{\mathrm{l}})]}. \tag{76}$$

From the continuity condition of T_{A} for $x = d_{\mathrm{l}}$, the relation specifying the length of the process zone is obtained

$$\cot[\lambda_{\mathrm{s}} d_{\mathrm{p}}] = \frac{\lambda_{\mathrm{s}}}{\lambda_{\mathrm{e}}} \tanh\left[\lambda_{\mathrm{e}} \left(\frac{l}{2} - d_{\mathrm{l}}\right)\right]. \tag{77}$$

As two process zones meet at $x = l/2$, their length $2d_{\mathrm{p}}$ then is

$$\cos[\lambda_{\mathrm{s}} d_{\mathrm{p}}) = 0, \qquad \lambda_{\mathrm{s}} d_{\mathrm{p}} = \pi/2, \qquad D_{\mathrm{p}} = 2d_{\mathrm{p}} = \frac{\pi}{\lambda_{\mathrm{s}}} \tag{78}$$

which is a characteristic value for the bi-layer system. The corresponding load value is specified by (74) with d_{l} replaced by d_{p}. As the length of process zone d_{l} increases, the load value decreases and its maximum corresponds to T^{C} or T^{D}.

Fig. 17 presents the progression of damage zone length d_{p} versus delamination part of the interface d_{l} for constant λ_{e} and different values of λ_{s}. The first part of the delamination process is associated with exit zones from the plate ends and next with partial decohesion of the layers. Fig. 18 presents evolution of the driving force T for increasing length d_{l} of delamination affected interface portion. Fig. 19 presents load-displacement responses during the progressing delamination process for different interface models discussed in the paper. The final process zone degradation is discussed in detail in the next section.

$$u_{\mathrm{A}}^{\mathrm{p}}(l)=\tau_{\mathrm{l}}^{\mathrm{C}}\frac{\lambda_{\mathrm{e}}\left[4E_{\mathrm{A}}h_{\mathrm{A}}+d_{\mathrm{l}}K_{\mathrm{t}}^{\mathrm{eff}}\left(3d_{\mathrm{l}}+\rho(2l-d_{\mathrm{l}})\right)\right]-2K_{\mathrm{t}}^{\mathrm{eff}}(2d_{\mathrm{l}}+l\rho)\tanh\left[\lambda_{\mathrm{e}}\left(d_{\mathrm{l}}-\frac{l}{2}\right)\right]}{4E_{\mathrm{A}}h_{\mathrm{A}}K_{\mathrm{t}}^{\mathrm{eff}}\lambda_{\mathrm{e}}}. \tag{82}$$

Box III.

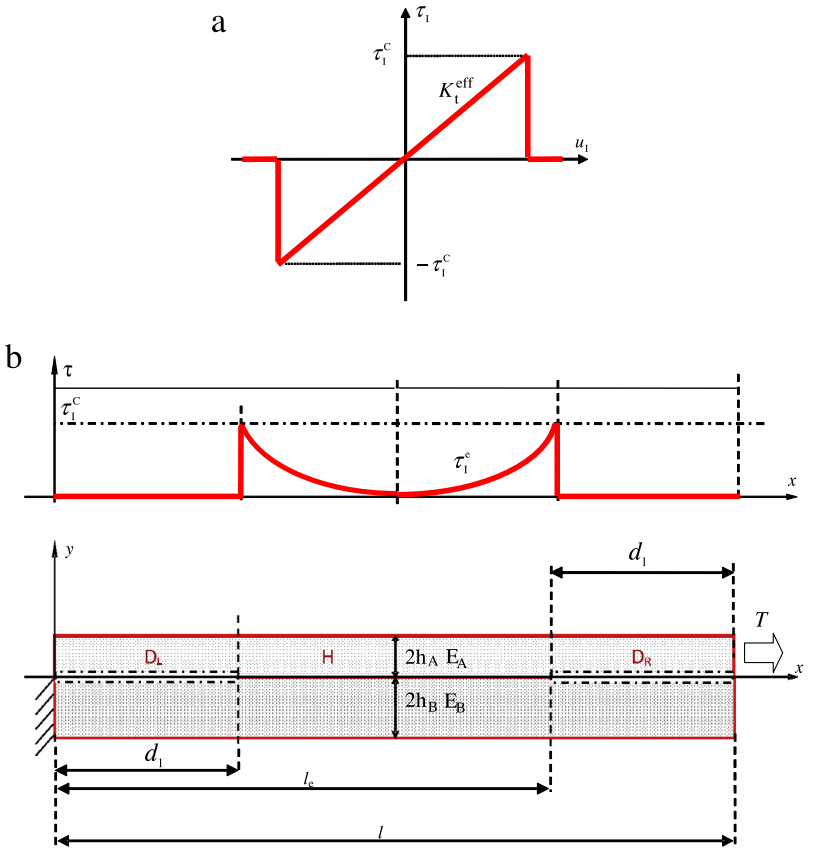

Fig. 20. Elastic–brittle interface model (a); shear stress field for growth of delamination in lap-joint system, (b).

4.2.3. Specific case 1: elastic-perfectly brittle bond model for $\rho=1$: $K_{\mathrm{s}}^{\mathrm{eff}}=\infty$

Referring to Fig. 20, for $K_{\mathrm{s}}^{\mathrm{eff}}=\infty$, the damage process zone does not exist. Then the elastic stress field (76) occurs in the central part and the condition $T_{\mathrm{A}}(d_{\mathrm{l}})=0$ is valid. We obtain from (76)

$$T^{\mathrm{C}}=\frac{2\tau_{\mathrm{l}}^{\mathrm{C}}}{\lambda_{\mathrm{e}}}\tanh\left[\lambda_{\mathrm{e}}\left(\frac{l}{2}-d_{\mathrm{l}}\right)\right] \tag{79}$$

and the load decreases during the whole process.

The displacement at the end of plate A is

$$u_{\mathrm{A}}^{\mathrm{D}}(l)=\frac{T}{4}\left(\frac{2d_{\mathrm{l}}}{E_{\mathrm{A}}h_{\mathrm{A}}}+\frac{1}{E_{\mathrm{B}}h_{\mathrm{B}}}-\frac{2\lambda_{\mathrm{e}}\coth\left[\lambda_{\mathrm{e}}\left(d_{\mathrm{l}}-\frac{l}{2}\right)\right]}{K_{\mathrm{t}}^{\mathrm{eff}}}\right). \tag{80}$$

4.2.4. Specific case 2: elastic-perfectly plastic model, $K_{\mathrm{s}}^{\mathrm{eff}}=0$

As the plastic zone $\tau_{\mathrm{l}}^{\mathrm{p}}=\tau_{\mathrm{l}}^{\mathrm{C}}$ is developed in the portion $0\le x\le l_{\mathrm{d}}$ and $T(l_{\mathrm{d}})=\tau_{\mathrm{l}}^{\mathrm{C}}l_{\mathrm{d}}$, Fig. 21, from (76) we obtain

$$T^{\mathrm{C}}=2\tau_{\mathrm{l}}^{\mathrm{C}}\left[d_{\mathrm{l}}+\frac{\tanh\left[\lambda_{\mathrm{e}}\left(\frac{l}{2}-d_{\mathrm{l}}\right)\right]}{\lambda_{\mathrm{e}}}\right] \tag{81}$$

and the displacement at the end of plate A is given in Box III.

4.3. Special case 3: rigid-softening model

4.3.1. Growth of process zones

For $\lambda_{\mathrm{e}}\to\infty$ two damage process zones are initiated after application of the increasing load T, Fig. 22. Denote the lengths of the right and left process zones by $d_{\mathrm{p}}^{\mathrm{l}}$ and $d_{\mathrm{p}}^{\mathrm{r}}$. Along the joint axis we have three segments $\mathrm{P_l}-\mathrm{H}-\mathrm{P_r}$, with the homogeneous stress state in the central H segment. The stress field in the process zone is expressed

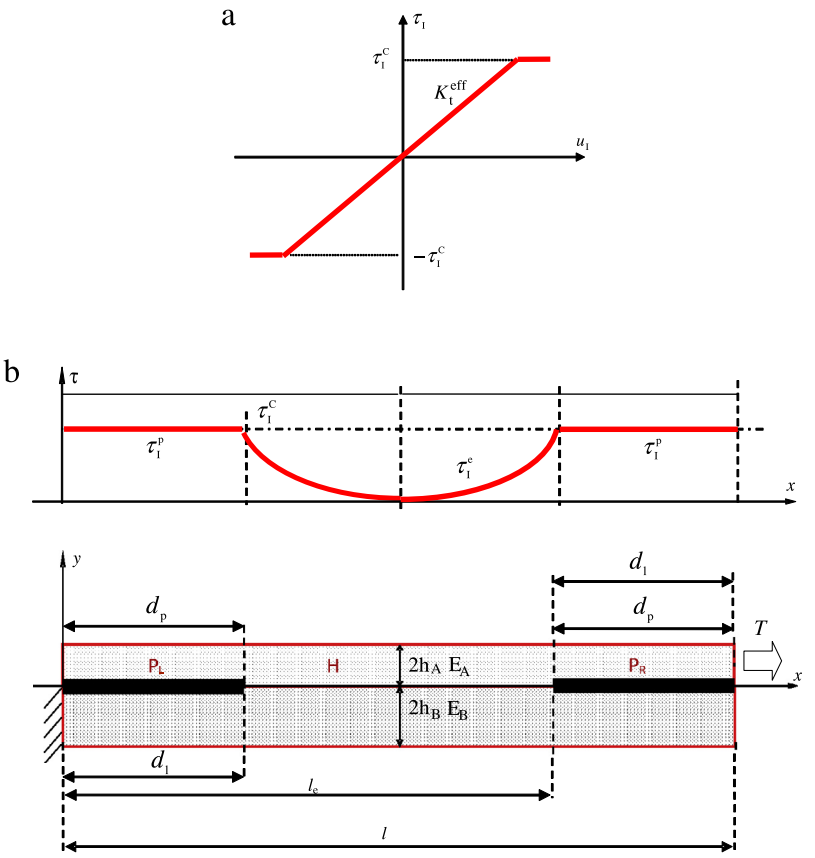

Fig. 21. Elastic-perfectly plastic interface model (a); substrate mechanical loading and shear stress field for motion of damage zone (b).

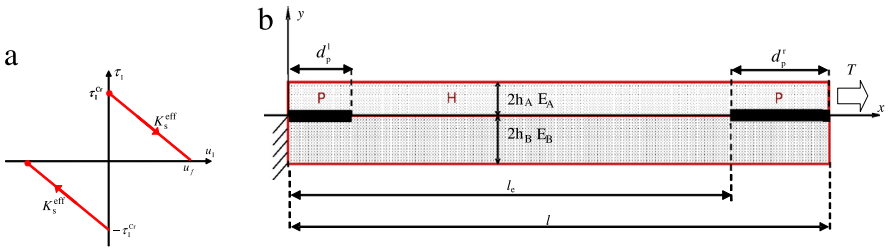

Fig. 22. The interface model (a), the lap-joint mechanical loading (b).

in (19), thus

$$
\begin{aligned}
u_{\mathrm{I}} &= D_1 \sin[\lambda_{\mathrm{s}} x] + D_2 \cos[\lambda_{\mathrm{s}} x] + \frac{\tau_{\mathrm{I}}^{\mathrm{C}}}{K_{\mathrm{s}}^{\mathrm{ef}}},\\
\tau_{\mathrm{I}} &= -K_{\mathrm{s}}^{\mathrm{ef}}(D_1 \sin[\lambda_{\mathrm{s}} x] + D_2 \cos[\lambda_{\mathrm{s}} x]),\\
T_{\mathrm{A}} &= \frac{K_{\mathrm{s}}^{\mathrm{ef}}}{\lambda_{\mathrm{s}}}(D_1 \cos[\lambda_{\mathrm{s}} x] - D_2 \sin[\lambda_{\mathrm{s}} x]) + D_3,\\
T_{\mathrm{B}} &= \frac{K_{\mathrm{s}}^{\mathrm{ef}}}{\lambda_{\mathrm{s}}}(-D_1 \cos[\lambda_{\mathrm{s}} x] + D_2 \sin[\lambda_{\mathrm{s}} x]) - E_{\mathrm{B}}/E_{\mathrm{A}} D_3,
\end{aligned}
\tag{83}
$$

where, D_1, D_2, D_3 are the integration constants.

In order to calculate the displacement fields $u_{\mathrm{B}}(x)$ and $u_{\mathrm{A}}(x)$, we start from the supported left end of plate B and determine its displacement in the segment $\mathrm{P_I} : 0 \leqslant x \leqslant d_{\mathrm{p}}^{\mathrm{I}}$, thus

$$
u_{\mathrm{B}}(x) = \int_0^{d_{\mathrm{p}}^{\mathrm{I}}} \frac{T_{\mathrm{B}}(x)}{2h_{\mathrm{B}} E_{\mathrm{B}}} \mathrm{d}x \tag{84}
$$

and next the displacement $u_{\mathrm{A}}(x)$ is determined as $u_{\mathrm{A}} = u_{\mathrm{I}} + u_{\mathrm{B}}$. The integration constants of (83) are specified from the boundary conditions

$$
\begin{aligned}
x = l_{\mathrm{e}} \quad &: \quad u_{\mathrm{I}} = u_{\mathrm{I}}' = 0\\
x = l \quad &: \quad T_{\mathrm{A}} = T, \qquad T_{\mathrm{B}} = 0\\
x = d_{\mathrm{p}}^{\mathrm{I}} \quad &: \quad u_{\mathrm{I}} = u_{\mathrm{I}}' = 0\\
x = 0 \quad &: \quad T_{\mathrm{A}} = 0, \qquad T_{\mathrm{B}} = T.
\end{aligned}
\tag{85}
$$

In the left damage zone P_l, $0 \leqslant x \leqslant d_p^l$ we have

$$\begin{aligned} u_l &= \frac{\tau_l^C}{K_s^{ef}}\left(1-\cos[\lambda_s(d_p^l-x)]\right),\\ \tau_l &= \tau_l^C\cos[\lambda_s(d_p^l-x)],\\ T_A &= \frac{\tau_l^C}{\lambda_s}(\sin[\lambda_s d_p^l]-\sin[\lambda_s(d_p^l-x)]),\\ T_B &= T-\frac{\tau_l^C}{\lambda_s}(\sin[\lambda_s d_p^l]-\sin[\lambda_s(d_p^l-x)]), \end{aligned} \tag{86}$$

and the displacement field takes the form

$$\begin{aligned} u_B(x) &= \frac{1}{2h_BE_B}\left[Tx-\frac{\tau_l^C}{\lambda_s}\left(\sin[\lambda_s d_p^l]x\right.\right.\\ &\quad\left.\left.-\frac{\cos[\lambda_s(d_p^l-x)]}{\lambda_s}+\frac{\cos[\lambda_s d_p^l]}{\lambda_s}\right)\right],\\ u_A(x) &= \frac{1}{2h_BE_B}\left[Tx-\frac{\tau_l^C}{\lambda_s}\left(\sin[\lambda_s d_p^l]x\right.\right.\\ &\quad\left.\left.-\frac{\cos[\lambda_s(d_p^l-x)]}{\lambda_s}+\frac{\cos[\lambda_s d_p^l]}{\lambda_s}\right)\right]\\ &\quad+\frac{\tau_l^C}{K_s^{ef}}\left(1-\cos[\lambda_s(d_p^l-x)]\right). \end{aligned} \tag{87}$$

In the homogeneous zone H, $d_p^l \leqslant x \leqslant l_e$ we have

$$u_l=\tau_l=0,\qquad T_A=T\frac{\rho}{1+\rho},\qquad T_B=T\frac{1}{1+\rho} \tag{88}$$

and displacement field is

$$\begin{aligned} u_B(d_p^l) &= \frac{1}{2h_BE_B}\left[Td_p^l-\frac{\tau_l^C}{\lambda_s}\left(\sin[\lambda_s d_p^l]d_p^l\right.\right.\\ &\quad\left.\left.-\frac{1}{\lambda_s}+\frac{\cos[\lambda_s d_p^l]}{\lambda_s}\right)\right], \end{aligned}$$

$$u_A(d_p^l)=u_B^e(d_p^l) \tag{89}$$

$$u_B(x)=u_B(d_p^l)+\frac{T}{2h_BE_B}\frac{x-d_p^l}{1+\rho},$$

$$u_A(x)=u_B(x). \tag{90}$$

In the right damage zone P_r, $l_e \leqslant x \leqslant l$ we have

$$\begin{aligned} u_l &= \frac{\tau_l^C}{K_s^{ef}}\left(1-\cos[\lambda_s(x-l_e)]\right),\\ \tau_l &= \tau_l^C\cos[\lambda_s(x-l_e)],\\ T_A &= T-\frac{\tau_l^C}{\lambda_s}(\sin[\lambda_s d_p^r]-\sin[\lambda_s(x-l_e)]),\\ T_B &= \frac{\tau_l^C}{\lambda_s}(\sin[\lambda_s d_p^r]-\sin[\lambda_s(x-l_e)]). \end{aligned} \tag{91}$$

Finally, we have

$$u_B(l_e)=u_B(d_p^l)+\frac{T}{2h_BE_B}\frac{l_e-d_p^l}{1+\rho}. \tag{92}$$

The force continuity conditions at the interfaces between the damage zones P_l, P_r and the homogeneous stress zone H provide two relations

$$\begin{aligned} u_B(x) &= u_B(l_e)+\frac{1}{2h_BE_B}\left[\frac{\tau_l^C}{\lambda_s}\left(\sin[\lambda_s d_p^r](x-l_e)\right.\right.\\ &\quad\left.\left.+\frac{\cos[\lambda_s(x-l_e)]}{\lambda_s}\right)\right],\\ u_B(l_e) &= u_B(l_e)\\ &\quad+\frac{1}{2h_BE_B}\left[\frac{\tau_l^C}{\lambda_s}\left(\sin[\lambda_s d_p^r]d_p^r+\frac{\cos[\lambda_s d_p^r]}{\lambda_s}\right)\right]. \end{aligned} \tag{93}$$

And finally

$$u_A(l)=u_B(l)+\frac{\tau_l^C}{K_s^{ef}}(1-\cos[\lambda_s d_p^r]). \tag{94}$$

Continuity condition at the interface between the damage zones d_p^l, d_p^r and the homogeneous stress zone H provide two relations:

$$\begin{aligned} T_A(l_e) &= \frac{\rho}{1+\rho}T \Rightarrow T_A(l_e)=T-\frac{\tau_l^C}{\lambda_s}\sin[\lambda_s d_p^r]\\ &= \frac{\rho}{1+\rho}T\\ T_A(d_p^l) &= \frac{\tau_l^C}{\lambda_s}\sin[\lambda_s d_p^l]=\frac{\rho}{1+\rho}T. \end{aligned} \tag{95}$$

The lengths of process zones d_p^l and d_p^r are now specified by the formulae

$$\begin{cases} \dfrac{\lambda_s}{\tau_l^C}\dfrac{1}{1+\rho}T=\sin[\lambda_s d_p^r]\\ \dfrac{\lambda_s}{\tau_l^C}\dfrac{\rho}{1+\rho}T=\sin[\lambda_s d_p^l] \end{cases} \Rightarrow \rho=\frac{\sin[\lambda_s d_p^l]}{\sin[\lambda_s d_p^r]}. \tag{96}$$

Thus, for $\rho > 1$ there is $d_p^l > d_p^r$ and for $\rho < 1$ there is $d_p^l < d_p^r$. In our analysis we consider the case $\rho < 1$ and $d_p^l < d_p^r$. The initiation of full delamination occurs when

$$\tau_l(l)=\tau_l^C\cos[\lambda_s d_p^r]=0. \tag{97}$$

The length of the process zone then reaches its critical value

$$\lambda_s d_p^r=\frac{\pi}{2},\quad d_p^r=\frac{\pi}{2}\frac{1}{\lambda_s} \tag{98}$$

and

$$\begin{aligned} T &= T_A=\frac{\tau_l^C}{\lambda_s}(1+\rho)\\ \tau_l(0) &= \tau_l^C\cos[\lambda_s d_p^l]=\tau_l^C\sqrt{1-\rho^2}. \end{aligned} \tag{99}$$

4.3.2. Process zone propagation

For $\rho < 1$, the full delamination starts to grow from the right end at constant force value expressed by (99) and for increasing displacement of plate A at $x = l$. The left process zone remains stagnant since $\tau_l(0) > 0$ remains fixed. Referring to Fig. 23, the stress state is specified by

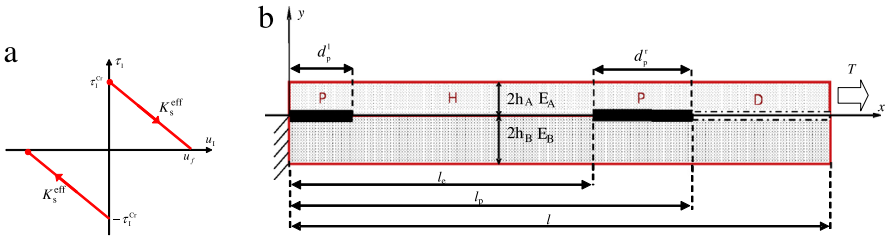

Fig. 23. The interface model (a), the lap-joint mechanical loading (b).

the same formulae (91) with replacement of l by l_p. The displacement field in consecutive zones is expressed by the following formulae:

In left damage zone (P_L), $0 \leqslant x \leqslant d_p^l$:

$$u_B(x) = \frac{1}{2h_B E_B}\left[Tx - \frac{\tau_I^C}{\lambda_s}\left(\sin[\lambda_s d_p^l]x - \frac{\cos[\lambda_s(d_p^l - x)]}{\lambda_s} + \frac{\cos[\lambda_s d_p^l]}{\lambda_s}\right)\right], \tag{100}$$

$$u_I(x) = \frac{\tau_I^C}{K_s^{ef}}\left(1 - \cos[\lambda_s(d_p^l - x)]\right),$$

$$u_A(x) = u_I(x) + u_B(x).$$

In the plate center zone (H), $d_p^l \leqslant x \leqslant l_e$:

$$u_B^e(d_p^l) = \frac{1}{2h_B E_B}\left[T d_p^l - \frac{\tau_I^C}{\lambda_s}\left(\sin[\lambda_s d_p^l]d_p^l - \frac{1}{\lambda_s} + \frac{\cos[\lambda_s d_p^l]}{\lambda_s}\right)\right], \tag{101}$$

$$u_A^e(d_p^l) = u_B^e(d_p^l)$$

$$u_A^e(x) = u_B^e(x),$$

$$u_B^e(x) = u_B^e(d_p^l) + \frac{T}{2h_B E_B}\frac{x - d_p^l}{1+\rho}. \tag{102}$$

In right damage zone (P_R), $l_e \leqslant x \leqslant l_p$:

$$u_B^e(l_e) = u_B^e(d_p^l) + \frac{T}{2h_B E_B}\frac{l_e - d_p^l}{1+\rho}, \tag{103}$$

$$u_B(x) = u_B^e(l_e) + \frac{1}{2h_B E_B}\left[\frac{\tau_I^C}{\lambda_s}\left(\sin[\lambda_s d_p^r](x - l_e) + \frac{\cos[\lambda_s(x - l_e)]}{\lambda_s}\right)\right], \tag{104}$$

$$u_B(l_p) = u_B^e(l_e) + \frac{1}{2h_B E_B}\frac{\tau_I^C}{\lambda_s}d_p^r$$

and

$$u_A(l_p) = u_B(l_p) + \frac{\tau_I^C}{\lambda_s}. \tag{105}$$

In the delaminated zone (D) $l_p \leqslant x \leqslant l$:

$$\begin{aligned} &u_B(x) = u_B(l_p), \qquad u_B(l) = u_B(l_p),\\ &u_A(x) = u_A(l_p) + T(x - l_p),\\ &u_A(l) = u_A(l_p) + T(l - l_p). \end{aligned} \tag{106}$$

4.3.3. Degradation of process zones

When the left and right damage process zones join each other at $x = d_p^l$, their total length equals $l_p = d_p^l + d_p^r$, Fig. 24. In the consecutive damage process the length l_p is assumed to remain fixed and the displacement discontinuity u_I to increase in the zone $0 \leqslant x \leqslant l_p$, thus

$$u_I(x) = \frac{\tau_I^C}{K_s^{ef}}(1 - \cos[\lambda_s(x - d_p^l)]) + u_1\cos[\lambda_s(x - d_p^l)], \tag{107}$$

where u_1 is the growing displacement discontinuity at $x = d_p^l$. The stress state in the damage process zone is now expressed as follows for $0 \leqslant x \leqslant l_p$

$$\begin{aligned} &\tau_I(x) = (\tau_I^C - K_s^{ef}u_1)\cos[\lambda_s(x - d_p^l)],\\ &T_A(x) = \frac{\tau_I^C - K_s^{ef}u_1}{\lambda_s}(\sin[\lambda_s d_p^l] - \sin[\lambda_s(d_p^l - x)]),\\ &T_B(x) = T - \frac{\tau_I^C - K_s^{ef}u_1}{\lambda_s}(\sin[\lambda_s d_p^l] - \sin[\lambda_s(d_p^l - x)]). \end{aligned} \tag{108}$$

Note that $\sin[\lambda_s d_p^r] = 1$ and $\sin[\lambda_s d_p^l] = \rho$, so for $x = l_p$ we have

$$\begin{aligned} &u_I(l_p) = \frac{\tau_I^C}{K_s^{ef}},\\ &T_A(l_p) = \frac{\tau_I^C - K_s^{ef}u_1}{\lambda_s}(1+\rho) = T, \qquad T_B(l_p) = 0. \end{aligned} \tag{109}$$

The degradation process proceeds for the decreasing load and increasing u_1 until $K_s^{ef}u_I = \tau_I^C$ and $T_A = 0$. The displacement field during the process zone degradation is

$$u_B(x) = \frac{1}{2h_B E_B}\frac{\tau_I^C - K_s^{ef}u_1}{\lambda_s}\left[x + \frac{\cos[\lambda_s(d_p^l - x)]}{\lambda_s} - \frac{\cos[\lambda_s d_p^l]}{\lambda_s}\right], \tag{110}$$

$$u_A(x) = u_B(x) + u_I(x)$$

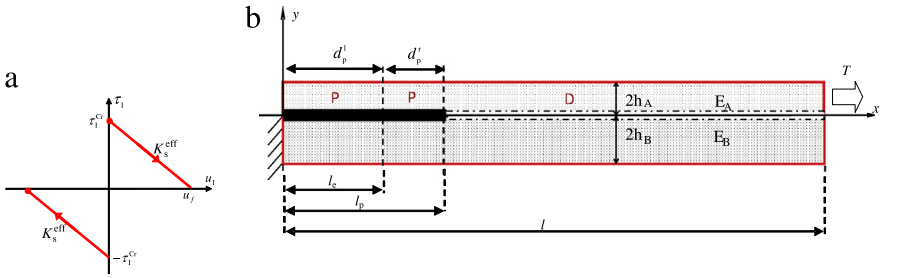

Fig. 24. The interface model (a), the lap-joint mechanical loading (b).

and the displacement of plate A at $x = l_p$ equals

$$u_A(l_p) = \frac{1}{2h_A E_A}\frac{1}{\lambda_s}\left[\frac{\tau_l^C}{\lambda_s}(1+\rho) + (\tau_l^C - K_s^{ef}u_1) \times \left(l_p - \frac{\sqrt{1-\rho^2}}{\lambda_s}\right)\rho\right]. \quad (111)$$

The displacement at the plate end is

$$u_A(l) = u_A(l_p) + \frac{(1+\rho)(l-l_p)}{2h_A E_A}\frac{\tau_l^C - K_s^{ef}u_1}{\lambda_s} = \frac{1}{2h_A E_A}\frac{1}{\lambda_s}\left[\frac{\tau_l^C}{\lambda_s}(1+\rho) + (\tau_l^C - K_s^{ef}u_1) \times \left(l + l\rho - l_p - \frac{\rho\sqrt{1-\rho^2}}{\lambda_s}\right)\right]. \quad (112)$$

The load–displacement diagram is identical to that presented in Fig. 14(b).

Note that

$$l_p = d_p^l + d_p^r = \frac{\beta}{\lambda_s}, \quad \beta = \frac{\pi}{2} + \arcsin[\rho]. \quad (113)$$

At the initial state of the degradation process, the displacement $u_1 = 0$ and then

$$\chi_u^l = \lambda_s u_A^l(l) = \frac{1}{2h_A E_A}\left[\frac{\tau_l^C}{\lambda_s}(1+\rho) + \tau_l^C\left(l + l\rho - \frac{\beta}{\lambda_s} - \frac{\rho\sqrt{1-\rho^2}}{\lambda_s}\right)\right]. \quad (114)$$

In the final failure state there is $\tau_l^C = K_s u_1$ and

$$\chi_u^f = \lambda_s u_A^f(l) = \frac{1}{2h_A E_A}\frac{\tau_l^C}{\lambda_s}(1+\rho) = \frac{T}{2h_A E_A} = \varepsilon_A^f, \quad (115)$$

where

$$\chi_u^l = \lambda_s u^l, \qquad \chi_u^f = \lambda_s u_A^f, \qquad \chi_l = \lambda_s l \quad (116)$$

are the non-dimensional displacement and lengths measures.

The snap-back response occurs when $u_A^l(l) > u_A^f(l)$ and then from (114) it follows that

$$\chi_l = \lambda_s l \geq \frac{1}{1+\rho}(\beta + \rho\sqrt{1-\rho^2}) = \chi_s. \quad (117)$$

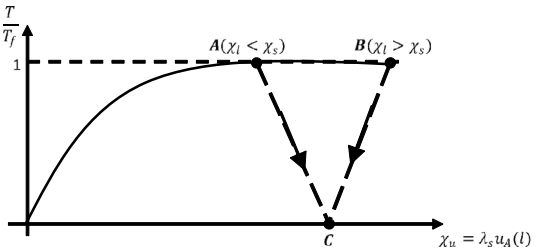

Fig. 25. The load displacement diagrams for joints of different lengths.

The inequality (117) specifies the length of joint for which the snap back response and uncontrolled dynamic failure occurs. On the other hand, for $\chi_l < \chi_s$, the displacement controlled static failure process will proceed. Fig. 25 illustrates the load–displacement response for joints of two lengths with the same strength and softening parameters. The limit load value is the same but the post-critical response depends on joint length. A similar analysis of the process zone degradation was presented in Ref. [44] for the fibre debonding problem and in Ref. [45,46] for the plate delamination problem with account for friction effect.

5. Discussion of analysis results

The analysis presented can be referred to laminated or joined composite structure and to geomechanical layer interaction of rock or soil strata systems. The specific cases treated analytically in the paper well illustrate the effect of material parameters K_t^{ef}, K_s^{ef}, τ_l^C on damage growth and delamination process. The elastic response is controlled by the parameter λ_e defined by Eq. (9) as the square root of ratio of the effective stiffness modulus of bonding layer to the stiffness modulus of interacting plates. Similarly, the stress distribution in the damage process zone and its length depend essentially on the softening stiffness parameter λ_s defined by (16). The alternative forms of these parameters are

$$\lambda_e = (K_t^{ef}C_p)^{\frac{1}{2}} = \left(\frac{K_t^{ef}}{S_p}\right)^{\frac{1}{2}} = \left(\frac{K_t^{ef}}{2h_B E_B}\frac{1+\rho}{\rho}\right)^{\frac{1}{2}},$$
$$\lambda_s = (K_s^{ef}C_p)^{\frac{1}{2}} = \left(\frac{K_s^{ef}}{S_p}\right)^{\frac{1}{2}} = \left(\frac{K_s^{ef}}{2h_B E_B}\frac{1+\rho}{\rho}\right)^{\frac{1}{2}}, \quad (118)$$

where, C_p denotes the plates compliance modulus and $S_p = C_p^{-1}$ denotes the stiffness modulus. It was

demonstrated that λ_e affects essentially the character of stress distribution. For large value of λ_e the transition to the uniform stress state occurs along a very short distance from the stress inhomogeneity. For rigid softening model, we have $\lambda_e \to \infty$. The damage and delamination growth then differ essentially from that proceeding for the elastic-softening model. The damage process zones of the constant length $d_p = \frac{\pi}{2}\frac{1}{\lambda_s}$ are generated at the plate ends and next translate along the contact interface at constant load, T_l. For the lap joint we have

$$T_l = \frac{\tau_l^C}{\lambda_s}(1+\rho) = \frac{\tau_l^C(1+\rho)}{(K_s^{\text{eff}}C_p)^{\frac{1}{2}}} = \left(\frac{2G_f}{C_p}\right)^{\frac{1}{2}}(1+\rho). \quad (119)$$

As T_l represents the limit load, it is seen that its value does not depend on the critical stress τ_l^C, but on the fracture energy and the plate compliance modulus. The scale effect is clearly demonstrated by specifying the average shear stress per unit length

$$\bar{\tau}^C = \frac{T_l}{l} = \frac{\tau_l^C}{\lambda_s}(1+\rho)\frac{1}{l} \quad (120)$$

which decreases with the length of plates.

The value of λ_s is also very important for specifying the limit load. The solutions for cases $\lambda_s = 0$ and $\lambda_s = \infty$ clearly illustrate the load dependence on this parameter. The reference is made to experimental testing of strength of joined composite elements by Ferraris et al.[53] and Ventrella et al.,[54] where the apparent shear strength of lap joints was determined, but the intrinsic parameters affecting adhesive joint thickness on the shear strength was examined in torsion, four point bending, single and double-lap tests. In fact, the varying joint thickness may affect the elastic and softening moduli K_t^{eff}, K_s^{eff} and parameters λ_e, λ_s controlling the interface stress distribution. The apparent joint strength measured as the averaged shear stress referred to the joint area is expressed by (120) for the rigid-softening model. In view of (119) if depends on the square root of the ratio of fracture energy and plates compliance. It is also inversely proportional to the joint length, l, thus demonstrating the scale effect. In the present paper it was assumed that the joint length is larger than the process zone length, so the process zone translation and length evolution can occur. The finite element elastic analysis presented[53,54] provides some information on the shear and peel stress distributions, however it is not satisfactory to clarify the mode of progressive damage and failure.

The elastic-softening model response well illustrates the evolution of the damage process zone. In the first example of substrate plate loading, the damaged zone length d_p decreases in the progressive delamination process. In the second example of lap joint the length of two zones d_p^l, d_p^r increases before their final degradation stage.

Let us refer to the numerical finite element analysis presented in papers by Alfano and Crisfield,[55] Goyal et al.[56] and Turon et al.[57] In Ref. [55] the interface constitutive model was formulated assuming linear elastic and softening responses, with numerical analysis of the opening failure mode of two layers under transverse loads. In Ref. [56] the delamination process of precracked beams in opening, shear and mixed modes was studied assuming the model with an exponential softening rule. In Ref. [57] the material parameter selection and the specification of the cohesive zone length was discussed for a bilinear elastic-softening model, identical to that used in this paper. The illustrative numerical examples of the layered composite delamination were next presented. The effective elastic stiffness modulus K_t^{eff} was recommended in Ref. [57] to be specified by the formula

$$hK_t^{\text{eff}} = \alpha E, \quad (121)$$

where, h and E are the averaged thickness and elastic modulus of bonded plates and $\alpha \geqslant 50$ is the proposed value of stiffness parameter, assuring sufficiently high value of K_t^{eff}. The values of K_t^{eff} based on literature data and resulting from (121) are in the range $K_t^{\text{eff}} = 4\,(10^5 \div 10^8)\,\frac{\text{N}}{\text{mm}^3}$. The length of the process zone was assumed as constant in the numerical analysis and specified from the Irwin formula

$$d_{cz} = M\frac{EG_f}{\tau_C^2} \quad (122)$$

where M is the parameter varying in the range $(0.2 \div 1.0)$ depending on the geometric joint parameters. This formula can be now compared with the cohesive zone length d_p specified by (98) for the rigid-softening model. In view of (118), we have

$$d_p = \frac{\pi}{2}\frac{1}{\lambda_s} = \frac{\pi}{2}\frac{1}{(K_s^{\text{eff}}C_p)^{0.5}} = \frac{\pi}{\tau_l^C}\left(\frac{E_A h_A G_f}{1+\rho}\right)^{0.5} \quad (123)$$

and the value of d_p specifies an upper bound on the length of process zone for an elastic-softening model.

Following the parameter data in Ref. [58] for a carbon fibre reinforced epoxy laminate

$$K_t^{\text{eff}} = 4\cdot 10^5\frac{\text{N}}{\text{mm}^3}, \qquad E = 150\ \text{GPa},$$
$$G_f = 0.352\frac{\text{N}}{\text{mm}}, \qquad \tau_l^C = 60\frac{\text{N}}{\text{mm}^2}$$

and assuming the bonded plate thickness $h_A = h_B = 5$ mm, we obtain from (118)–(123)

$$\lambda_s = 82.5\frac{1}{\text{m}}, \qquad \lambda_e = 730\frac{1}{\text{m}}, \qquad K_s^{\text{eff}} = 5113\frac{\text{N}}{\text{mm}^3},$$
$$d_{cz} = 11.73\ \text{mm}, \qquad d_p = 19.03\ \text{mm}.$$

The large value of λ_e indicates that there is very fast transition from the inhomogeneous stress state in the process zone to the uniform stress state and the solution for the rigid-softening model well describes the damage process. Then the developed process zone length $d_p = \frac{\pi}{2\lambda_s}$ remains constant during zone propagation. The similar conclusion was reached in the numerical analysis in Ref. [58], indicating that the constant length assumption of the process zone is legitimate and the maximal load at failure does not depend on the τ_l^C value. Note that d_p predicted by (123) is larger than d_{cz} predicted by the Irwin formula, as it constitutes the upper bound on the cohesive zone length.

Referring to rock mechanics the mode of localized shear failure is fundamental in the compressive stress regime.

The delamination process of bi-layer system can occur when one layer deforms excessively relative to adjacent layers under increasing stress and induces large shear stress at the interface. The first example of substrate loading can then provide the insight into the delamination mode. The elastic stiffness of interface bond now depends on the normal pressure. Assume the following parameters following Morache et al.[58]

$$K_t^{\text{eff}} = 20 \cdot \frac{\text{MPa}}{\text{mm}}, \qquad E = 70\ \text{GPa},$$

$$G_f = 0.07 \frac{\text{N}}{\text{mm}}, \qquad \tau_l^{\text{C}} = 5\ \text{MPa}, \qquad h = 50\ \text{mm}.$$

Now the calculated model parameters and process zone lengths are

$$\lambda_e = 2.39 \frac{1}{\text{m}}, \qquad \lambda_s = 7.14 \frac{1}{\text{m}}, \qquad d_{cz} = 0.156\ \text{m},$$

$$d_p = 0.219\ \text{m}.$$

The extended analysis of delamination process of a plate under lateral compressive stress with account for damage and sliding friction effect was presented by Białas and Mróz.[45,46]

Acknowledgments

The research work presented in the paper has been carried out within the project: "Experimental and numerical analysis of coupled deterministic-statistical size effect in brittle materials" financed by National Research Centre NCN (UMO-2013/09/B/ST8/03598).

References

[1] Parker AP. Stability of multiple edge cracks. *Eng Fract Mech*. 1999;62:577–591.
[2] Chi S, Chung Y-L. Cracking in coating-substrate composite with multi-layered and FGM coatings. *Eng Fract Mech*. 2003;70:1227–1243.
[3] Chung YL, Pon C-F. Boundary element analysis of cracked film–substrate media. *Internat J Solids Struct*. 2001;38:75–90.
[4] Zhang T-Y, Zhao M-H. Equilibrium depth and spacing of cracks in a tensile residual stressed thin film deposited on a brittle substrate. *Eng Fract Mech*. 2002;69:589–596.
[5] Erdem Alaca B, Saif MTA, Sehitoglu Huseyin. On the interface debond at the edge of a thin film on a thick substrate. *Acta Mater*. 2002;50:1197–1209.
[6] Kokini K, Takeuchi YR. Multiple surface thermal fracture of graded ceramic coatings. *J Thermal Stresses*. 1998;27:715–725.
[7] Thouless MD, Evans AG, Ashby MF, Hutchinson JW. The edge cracking and spalling of brittle plates. *Acta Metall*. 1987;35:1333–1341.
[8] Thouless MD, Evans AG. Comment on the spalling and edge cracking of plates. *Scr Metall Mater*. 1990;124:1507–1510.
[9] Agrawal DC, Raj R. Measurement of the ultimate shear strength of a metal–ceramic interface. *Acta Metall*. 1989;37:1265–1270.
[10] Kim S-R, Nairn JA. Fracture mechanics analysis of coating/substrate systems. Part I: Analysis of tensile and bending experiments. *Eng Fract Mech*. 2000;65:573–593. Kim.
[11] Kim S-R, Nairn JA. Fracture mechanics analysis of coating/substrate systems. Part II: Experiments in bending. *Eng Fract Mech*. 2000;65:595–607.
[12] Schulze GW, Erdogan F. Periodic cracking of elastic coating. *Internat J Solids Struct*. 1998;35:3615–3634.
[13] Nairn JA. The strain energy release rate of composite microcracking: a variational approach. *J Compos Mater*. 1989;23:1106–1129.
[14] Nairn JA, Kim S-R. A fracture mechanics analysis of multiple cracking in coatings. *Eng Fract Mech*. 1992;42:195–208.
[15] Hu MS, Evans AG. The cracking and decohesion of thin films on ductile substrates. *Acta Metall*. 1989;37:917–925.
[16] Timm DH, Guzina BB, Voller VR. Prediction of thermal crack spacing. *Internat J Solids Struct*. 2003;40:125–142.
[17] Hutchinson JW, Suo Z. Mixed mode cracking of layered materials. In: Hutchinson JW, Wu TY, eds. *Advances in Applied Mechanics*. Academic Press; 1991:63–191.
[18] Evans SL, Gregson PJ. The effect of a plasma-sprayed hydroxyapatite coating on the fatigue properties of Ti-6Al-4V. *Mater Lett*. 1993;16:270–274.
[19] Forrest DJ, Shelton JC, Gregson PJ. Fatigue failure in a plasma sprayed hydroxyapatite coated titanium alloy. In: *Proceedings of the Fifth World Biomaterials. Congress Toronto*. University of Toronto Press; 1996:324.
[20] Holtz RL, Sadananda K. Fatigue behaviour of nanostructured and conventional coatings. In: Berndt CC, ed. *Abstracts from Thermal Spray Processing of Nanoscale Materials II*. New York: United Engineering Foundation; 1999:30–32.
[21] Shaw MC, Marshall DB, Dalgleish BJ, Dadkhad MS, He MY, Evans AG. Fatigue crack growth and stress redistribution at interfaces. *Acta Metall Mater*. 1994;42:4091–4099.
[22] Mróz KP, Doliński K. The crack growth prediction in homogeneous materials and bimaterial systems. *J Appl Math Mech*. 2010;90:721–744.
[23] Suresh S, Sugimara Y, Tschegg EK. The growth of a fatigue crack approaching a perpendicularly oriented bimaterial interface. *Scr Metall Mater*. 1992;27:1189–1194.
[24] Sugimara Y, Suresh S. Fatigue of coated materials. In: *Proceedings of the 1993 ASME Winter Annual Meeting*. New York: American Society of Mechanical Engineers; 1993:9.
[25] Sugimara Y, Lim PG, Shih CF, Suresh S. Fracture normal to a bimaterial interface: effects of plasticity on crack-tip shielding and amplification. *Acta Metall Mater*. 1995;43:1157–1169.
[26] Suresh S, Sugimara Y, Ogawa T. Fatigue cracking in coated materials with brittle surface coatings. *Scr Metall Mater*. 1993;29:237–242.
[27] Volkersen O. Die Nietkraftvereilung von zugbeanspruchten Nietverbindungen mit konstante Laschenuerschnitten. *Luftfahrtforschung*. 1938;1–2:41–47.
[28] Cox LH. The elasticity and strength of paper and other fibrous materials. *Br J Appl Phys*. 1952;3:72–79.
[29] Hedgepeth JM. Stress concentrations in filamentary structures. NASA TN D-882, 1961.
[30] Kelly A, Tyson WR. Tensile properties of fibre reinforced metals:Copper/tungsten and copper/molybdenum. *J Mech Phys Solids*. 1965;13:329–338.
[31] Dugdale DS. Yielding of steel sheets containing slits. *J Mech Phys Solids*. 1960;8:100–104.
[32] Barenblatt GI. The mathematical theory of equilibrum cracks in brittle fracture. In: *Advances in Applied Mechanics, Vol. 7*. New York: Academic Press; 1962:55–129.
[33] Tvergaard V, Hutchinson JW. The relation between crack growth resistance and fracture process parameters in elasticplastic solids. *J Mech Phys Solids*. 1992;40:1377–1397.
[34] Cui W, Wisnom MR. A combined stress-based and fracture-mechanics-based model for predicting delamination in composites. *Composites*. 1993;24:467–474.
[35] Needleman A. A continuum model for void nucleation by inclusion debonding. *J Appl Mech*. 1987;54:525–532.
[36] Xu X-P, Needleman A. Numerical simulations of fast crack growth in brittle solids. *J Mech Phys Solids*. 1994;42(9):1397–1434.
[37] De Moura MFSF, Chousal JAG. Cohesive and continuum damage models applied to fracture characterization of bonded joints. *Int J Mech Sci*. 2006;48:493–503.
[38] De Moura MFSF, Campilho RDSG, Gonçalves JPM. Pure mode II fracture characterization of composite bonded joints. *Internat J Solids Struct*. 2009;46:1589–1595.
[39] Petrossian Z, Wisnom MR. Prediction of delamination initiation and growth from discontinuous plies using interface elements. *Compos A: Appl Sci Manuf*. 1998;29A:503–515.
[40] Pinho ST, Ianucci L, Robinson P. Formulation and implementation of decohesion elements in an explicit finite element code. *Compos A: Appl Sci Manuf*. 2006;37:778–789.
[41] Camanho PP, Dávila CG. Mixed-mode decohesion finite elements for the simulation of delamination in composite materials. NASA/TM-2002-211737, 2002.
[42] Alfano M, Furgiuele F, Leonardi A, Maletta C, Paulino GH. Mode I fracture of adhesive joints using tailored cohesive zone models. *Int J Fract*. 2009;157:193–204.
[43] Williams JG, Hadavinia H. Analytical solutions for cohesive zone models. *J Mech Phys Solids*. 2002;50:809–825.
[44] Schreyer HL, Peffer A. Fiber pull-out based on one-dimensional model of decohesion. *Mech Mat*. 2000;32:821–836.

[45] Mróz Z, Białas M. A simplified analysis of interface failure under compressive normal stress and monotonic ar cyclic shear loading. *Int J Numer Anal Geomech*. 2005;29:337–368.
[46] Białas M, Mróz Z. Modelling of progressive interface failure under combined normal compression and shear stress. *Internat J Solids Struct*. 2005;42:4436–4467.
[47] Białas M, Mróz Z. An energy model of segmentation cracking of thin films. *Mech Mater*. 2007;39(9):845–864.
[48] Białas M, Majerus P, Herzog R, Mróz Z. Numerical simulation of segmentation cracking in thermal barrier coatings by means of cohesive zone elements. *Mater Sci Eng A-Mat Prop Microstr Process*. 2005;412(40910):241–251.
[49] Białas M, Mróz Z. Crack patterns in thin layers under temperature loading. Part I: Monotonic loading. *Eng Fract Mech*. 2006;73: 917–938.
[50] Ivanova J, Valeva V, Mróz Z. Mechanical modelling of the delamination of bi-material plate structure. *J Theoret Appl Mech*. 2006;36: 39–54.
[51] Nikolova G, Ivanova J, Mróz Z. Modelling of thermally induced progressive delamination in two-plate structure. *J Theoret Appl Mech*. 2006;36:71–92.
[52] Goglio L, Rosetto M. Precision of the one-dimensional solutions for bonded double lap joints. *Int J Adhesion Adhesives*. 2011;31:301–314.
[53] Ferraris M, Ventrella A, Salvo M, Avalle M, Pavia F, Martin E. Comparison of shear strength tests on AV119 epoxy–joined carbon/carbon composites. *Composites B*. 2010;41:182–191.
[54] Ventrella A, Salvo M, Avalle M, Ferraris M. Comparison of shear strength tests on AV119 epoxy–joined ceramics. *J Mater Sci*. 2010; 45(16):4401–4405.
[55] Alfano G, Crisfield MA. Finite element models for delamination analysis of laminated compistes: mechanical and computational issues. *Internat J Numer Methods Engrg*. 2001;50:1701–1736.
[56] Goyal VG, Johnson ER, Davila CG. Irreversible constitutive law for modelling the delamination process using interfacial surface discontinuities. *Comput Structures*. 2004;65:289–305.
[57] Turon A, Davila CG, Camanho PP, Costa J. An engineering solution for mesh size effects in the simulation of delamination using cohesive zone models. *Eng Fract Mech*. 2007;74:1665–1682.
[58] Morache A, Riss J, Geutier S. Experimental and modelled behaviour of a rock fracture under normal stress. *Rock Mech Rock Eng*. 2008;41: 869–892.